remote sensing

MDPI

Article

Insights into the Magmatic Feeding System of the 2021 Eruption at Cumbre Vieja (La Palma, Canary Islands) Inferred from Gravity Data Modeling

Fuensanta G. Montesinos [1,2,*], Sergio Sainz-Maza [2,3], David Gómez-Ortiz [4], José Arnoso [2,5], Isabel Blanco-Montenegro [2,6], Maite Benavent [1,2], Emilio Vélez [2,5], Nieves Sánchez [7] and Tomás Martín-Crespo [4]

1 Facultad de CC. Matemáticas, Universidad Complutense de Madrid, Plaza de Ciencias 3, 28040 Madrid, Spain
2 Research Group 'Geodesia', Universidad Complutense de Madrid, 28040 Madrid, Spain
3 Observatorio Geofísico Central (IGN), C/Alfonso XII, 3, 28014 Madrid, Spain
4 Departmento de Biología y Geología, Física y Química Inorgánica, ESCET, Universidad Rey Juan Carlos, C/Tulipán s/n, Móstoles, 28933 Madrid, Spain
5 Instituto de Geociencias (IGEO, CSIC-UCM), C/Doctor Severo Ochoa, 7, 28040 Madrid, Spain
6 Departmento de Física, Escuela Politécnica Superior, Universidad de Burgos, Avda. de Cantabria s/n, 09006 Burgos, Spain
7 Instituto Geológico y Minero de España (IGME, CSIC), Unidad Territorial de Canarias, Alonso Alvarado, 43, 2A, 35003 Las Palmas de Gran Canaria, Spain
* Correspondence: fuensant@ucm.es

Abstract: This study used spatiotemporal land gravity data to investigate the 2021 eruption that occurred in the Cumbre Vieja volcano (La Palma, Canary Islands). First, we produced a density model by inverting the local gravity field using data collected in July 2005 and July 2021. This model revealed a low-density body beneath the western flank of the volcano that explains a highly fractured and altered structure related to the active hydrothermal system. Then, we retrieved changes in gravity and GNSS vertical displacements from repeated measurements made in a local network before (July 2021) and after (January 2022) the eruption. After correcting the vertical surface displacements, the gravity changes produced by mass variation during the eruptive process were used to build a forward model of the magmatic feeding system consisting of dikes and sills based on an initial model defined by the paths of the earthquake hypocenters preceding the eruption. Our study provides a final model of the magma plumbing system, which establishes a spatiotemporal framework tracing the path of magma ascent from the crust–mantle boundary to the surface from 11–19 September 2021, where the shallowest magma path was strongly influenced by the low-density body identified in the inversion process.

Keywords: volcano plumbing systems; geophysical methods; four-dimensional gravimetry; inverse and forward model; La Palma 2021 eruption

Citation: Montesinos, F.G.; Sainz-Maza, S.; Gómez-Ortiz, D.; Arnoso, J.; Blanco-Montenegro, I.; Benavent, M.; Vélez, E.; Sánchez, N.; Martín-Crespo, T. Insights into the Magmatic Feeding System of the 2021 Eruption at Cumbre Vieja (La Palma, Canary Islands) Inferred from Gravity Data Modeling. *Remote Sens.* **2023**, *15*, 1936. https://doi.org/10.3390/rs15071936

Academic Editors: Raffaele Castaldo, Umberto Riccardi and Stefano Carlino

Received: 5 February 2023
Revised: 24 March 2023
Accepted: 1 April 2023
Published: 4 April 2023

1. Introduction

Volcanic hazard assessment is conditioned by the understanding of the geological structure, tectonic setting and subsurface processes taking place inside an active volcano [1]. The analysis and interpretation of gravity observations made on Earth's surface can contribute to the study of volcanic processes in two significant ways. First, the inversion of spatial gravity variations produces subsurface density models. Thus, it is possible to build a density contrast model of the crust and upper mantle, which is usually involved in the evolution of volcanic processes. Second, gravimetry allows for the study of geodynamic processes based on spatiotemporal gravity changes [2]. Repeated observations made in different stages of the volcanic process (before, during or after an eruption) help in interpreting the redistribution of masses involved in the process. The recent volcanic episode

that occurred in La Palma in 2021 on the western flank of the Cumbre Vieja volcano provides an excellent opportunity to apply these gravimetric techniques using several gravity datasets acquired both before and after the eruption occurring from 19 September to 13 December 2021.

Potential field methods have been widely used to study volcanic islands to obtain 3D models of the inner volcanic systems to image magma intrusion beneath the surface. This allows us to delineate the main volcanic structures and constrain the locations of dense intrusive basaltic and ultramafic bodies, as well as geothermal areas, related to the heat flow along the plumbing system (e.g., [3–10]).

La Palma is one of the youngest islands of the Canary Islands, and it is an intraplate volcanic archipelago located close to the NW coast of the African continent. The island is located in the westernmost part of the archipelago, covering an emerged area of 708 km^2 (Figure 1). The insular volcanic edifice developed from 4000 m below sea level up to 2400 m above sea level; and overlies an old oceanic lithosphere (Jurassic age, magnetic reversal isochron M25, 156 Ma) [11]. The seamount stage started ~4–3 Ma ago, resulting in the construction of a basaltic Pliocene submarine edifice comprising a gabbroic plutonic complex [12] that presently outcrops to the north of the island (Figure 1, Basal complex). Subaerial volcanism started 1.8 Ma ago and built several volcanic edifices (Garafia, Taburiente, Cumbre Nueva and Bejenado), which developed in the northern part of the island after successive stages, and building periods alternated with large flank collapses. Volcanic activity paused ~0.4 Ma ago, and after an erosion period, the activity migrated south [12,13]. This last stage (from ~125 ka to the present) corresponds to the development of the Cumbre Vieja edifice (e.g., [14,15]) (Figure 1). Subaerial volcanic activity is mainly represented by basaltic, basanitic and tephritic lava flows and pyroclastic deposits produced by successive Strombolian eruptions (e.g., [12]).

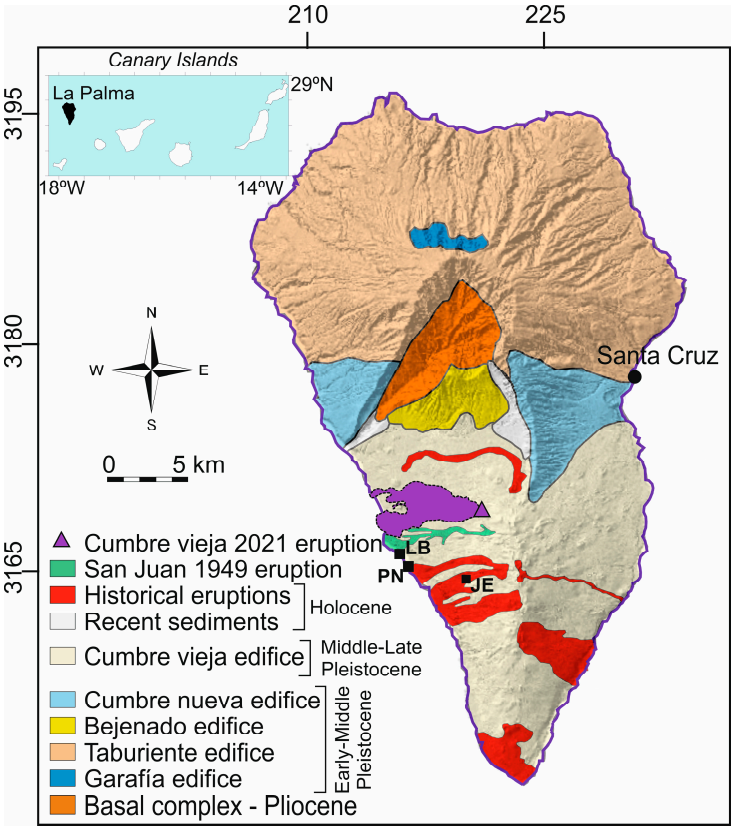

Figure 1. Simplified geological map of the island of La Palma, including historical eruptions and the last eruption in 2021 at Cumbre Vieja. UTM coordinates are in km, in zone 28. Black squares denote the villages of Puerto Naos (PN), La Bombilla (LB) and Jedey (JE).

In this paper, we study the latest eruption that took place in La Palma in 2021 from the study of gravimetric data observed before and after the eruption. Using a new gravimetric dataset obtained in the area around the eruption in July 2021, in combination with previous terrain and marine gravity data, we obtained a new Bouguer anomaly map. Then, we built a 3D density structure model for the Cumbre Vieja area using a genetic algorithm for the inversion of gravity data [16]. We interpret these data jointly with information derived from previous structural models obtained from our gravity data, seismic tomography [17] and magnetotellurics [18]. Additionally, a new gravity survey carried out in January 2022 allowed us to calculate gravity variations with respect to July 2021, resulting in the creation of a dynamic image of mass changes resulting from the eruption. We propose a model of the magma path through the crust, consisting of different dikes and sills, obtained from the distribution of seismic data and the best fit between theoretical and observed space-time gravity variations. Finally, we discuss the structural influence on the path followed by the magma until it reaches the surface according to the obtained models.

2. The 2021 Volcanic Eruption in La Palma

The 2021 eruption at the Cumbre Vieja rift lasted 85 days, from 19 September to 13 December, becoming the longest historical eruption in La Palma. The elongated fissure eruption at N133°E built a volcanic cone with a maximum height of 200 m from preexisting topography, reaching up to 1121 m above sea level. The lava emerged from six major craters and up to nine minor vents [19]. The maximum distance between the eruptive centers was approximately 1 km, and not all the vents were active at the same time; rather, their activity alternated according to temporal variations in the eruptive process. The final estimated erupted lava volume was approximately 34×10^6 m^3, covering an area of 12 km^2 [19].

Seismicity, ground deformation and degassing often precede volcanic eruptions [20]. Several studies have pointed to deformation patterns existing prior to La Palma's seismic unrest in September 2021. Since the 1990s, movements on the west flank of the island, as well as around the Teneguía volcanic edifice, have been reported and attributed to deflation episodes [21–26]. In addition, [27] evidenced changes in the geochemical features of the volcanic system, involving substantial increases in CO_2 emissions during 2011 and 2013 around the Cumbre Vieja edifice. More recently, [28] reported changes in helium isotope ratios as an early precursor of the volcanic eruption, pointing to the period of 2008–2013 as the start of the reactivation. However, none of these studies showed strong evidence of an emerging volcanic process.

According to the Spanish National Geographic Institute (IGN) seismic catalog (https://doi.org/10.7419/162.03.2022 (accessed on 1 July 2022), several seismic swarms occurred between October 2017 and August 2021 in La Palma. The earthquakes, with an approximate east–west trend, were located at depths between 14 and 30 km below sea level. The first seismic swarm was followed by nine similar swarms occurring from February 2018 to August 2021. Geochemical anomalies in gases, such as Rn, H and CO_2, which were observed between the first two seismic swarms, as per [29], were the first to signal reactivation under Cumbre Vieja. Subsequently, ref. [15] also reported the unrest stage of La Palma from the detection of deformation patterns in the Aridane Valley, probably between 2009 and 2010, based on InSAR images. Recently, ref. [30], using InSAR observations, identified the possibility of shallow magma accumulation 3.5 months before the eruption, several kilometers SSW of the main emission area.

The seismic catalog provided by the IGN revealed a new seismic swarm starting on 11 September 2021, which was shallower than in previous cases. After a quick upward migration of the hypocenters from 10–12 km up to 2–3 km and then to the surface (Supporting Information, Figure S1), a volcanic eruption started on 19 September from a vent located approximately 2 km northwest of the 1949 historical San Juan eruption (Figure 1). This new eruption was also preceded by a ground uplift of approximately 30 cm in the vicinity of the eruptive center, as detected by InSAR [31]. After the end of the eruptive process on 13 December, intense gas emissions still affected two villages on

the western coast of La Palma: La Bombilla and Puerto Naos (Figure 1). By the end of November 2021, very high concentrations of CO_2 were measured in these two localities, which were evacuated at the beginning of the eruption due to the hazard of isolation by rockfalls cutting off access to roads to these localities. At present (March 2023), these two localities remain evacuated due to high concentrations of CO_2. This gas principally concentrates in basements and garages in the interiors of buildings and on the outside, with values that locally exceed 100.000 ppm, as detected by a permanent monitoring network (https://volcan.lapalma.es/pages/calidad-del-aire (accessed on 1 February 2023). These anomalous high CO_2 concentrations have a volcanic hydrothermal origin [32] and prevent people from returning home.

Earthquake hypocenters are the most reliable means to infer the magma location and allow for the tracking of the real-time position of magma at depth. Ground deformation, geochemical changes and petrology studies help provide a complete account of the process. Based on these data, some previous eruptive models were imaged for this last volcanic process that occurred at La Palma [30,31]. Thus, early seismicity at depth delineated the upper limit of the reservoir, probably located at the Moho depth, which ascended through the crust in the week before the onset of the eruption. Following a westerly direction, it probably stopped and formed a sill at 5 km below sea level, according to the deformation model provided by [31]. Finally, the ascending magma crossed the hydrothermally altered zone described by [18]. De Luca et al. in [31] show, from analysis of DInSAR images, a process of magma rising through a system of interconnected sills and dikes and propose the existence of two feeder dikes, which is compatible with the observed deformation patterns that would represent the ascending magma path.

3. Data and Methods

3.1. GNSS Data

To study the surface displacements preceding the eruption onset, when a significant increase in the seismic events took place, and during the first two weeks of the eruptive process, we analyzed data from available permanent GNSS stations in La Palma (LP01, LPAL from IGN, and MAZO from the GRAFCAN-Government of Canary Islands), as well as from our BALN station located on El Hierro Island [33] (Figure 2). We used the precise point positioning (PPP) technique to process the data [34]. The results reveal increases of ~3.5 cm and 2.5 cm in the LP01-LPAL and LP01-MAZO baselines, respectively, and a decrease in the LPAL-MAZO baseline of ~1 cm. Additionally, the analysis suggests a remarkable decrease of ~3 cm in the BALN-LP01 baseline (Figure 2). In addition, the computed horizontal displacements are in the range of 2 to 4 cm for stations LP01 and MAZO, whereas the maximum ground uplift detected at LP01 was ~1.5 cm.

Moreover, we analyzed GNSS data from surveys carried out during the observation of the gravity network in July 2021 and January 2021 to map the deformation pattern between these two gravity surveys (see Sections 3.2 and 3.4).

3.2. Gravity Data Collection

The first gravity survey was carried out in July 2005 in the southern part of La Palma. We measured 101 gravity stations using a LaCoste and Romberg model-G gravimeter with digital electronic reading, considering an average equidistance of 1–1.5 km between them (Figure 3). A second survey was performed using a Scintrex CG5 gravimeter in July 2021, covering the central area of Cumbre Vieja with 41 new gravity stations. Initially, we selected 31 stations to establish a control network to monitor the eruptive area of Cumbre Vieja, although some of them became inaccessible due to lava flows or ash fall deposits produced by the 2021 eruption (Figure 3).

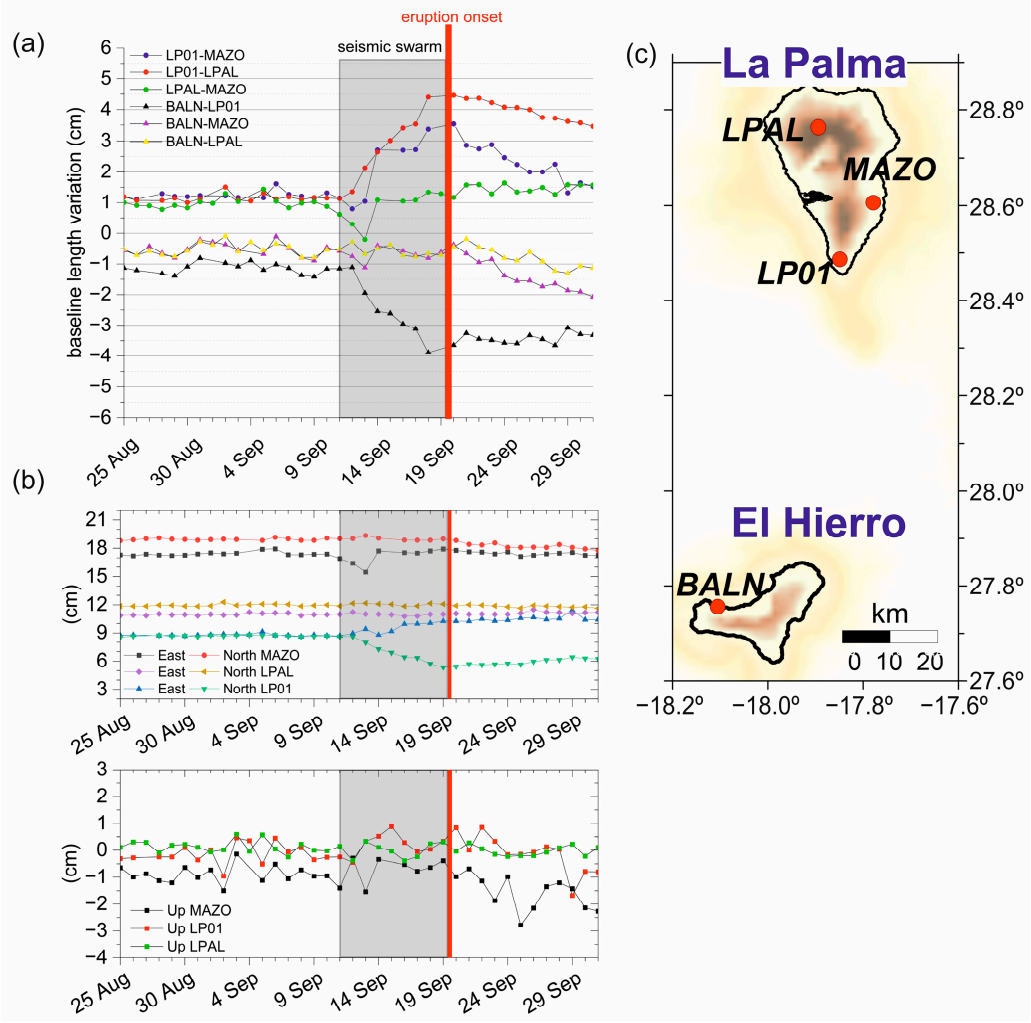

Figure 2. (**a**) Variation in the baseline length calculated for GNSS stations LP01, LPAL and MAZO situated in La Palma and station BALN in El Hierro. (**b**) Variation in the local east, north and upward coordinates for GNSS stations LP01, LPAL and MAZO in La Palma. The gray shaded areas in (**a**,**b**) indicate the period of the seismic swarm prior to the eruption onset (red line). *Y*-axis units are shifted for easier viewing. (**c**) Maps of the La Palma (the black area indicates the 2021 lava flows) and El Hierro islands, showing the distribution of GNSS stations (red dots).

In January 2022, after the 2021 eruption had ended, we remeasured stations of this gravity network. Only 15 stations of the initial network could be recovered (Figure 3 and Table S1 in the Supporting Information).

We reobserved approximately 25% of the stations in each survey and occupied a selected base station at least twice daily. All these repeated observations were used to control instrumental drift and possible jumps or errors during the observation process. Three absolute gravity stations (PALM_ENIC, PALM_EANT and PALM_EVIR in Figure 3) provided by the Spanish IGN (Supporting Information, Table S2) were also observed and were used as reference stations.

Each station at nearly 30′ was occupied, and one gravity reading per minute was collected. The standard deviation of the single readings was within the interval of (0.01, 0.08) mGal (1 mGal = 10^{-5} m s^{-2}). Gravity data were reduced by the height of the instrument over the benchmark. In addition, these values were corrected for atmospheric effects and Earth tides using the models provided by [35].

The precise coordinates of all stations were obtained by differential GNSS calculation, with an average error associated with the height values of ~2.6 cm, which can be translated as a gravity error of ~8 μGal (1 μGal = 10^{-8} m s^{-2}).

We independently processed the two campaigns carried out before the eruption (July 2021) and after the eruption (January 2022). We estimate a linear component of the instrumental drift for each survey and the gravity value for each station using a least squares adjustment. In this procedure, the drift correction was applied for all gravity observations. The adjustment of the observations gave standard deviations of 0.026 mGal and 0.045 mGal for the respective datasets obtained in July 2021 and January 2022. Weather conditions and some instability due to eventual seismicity during the observation period could explain this latter value, which is higher than the value obtained for the July 2021 survey. Finally, we selected the absolute station PALM_EVIR, which is located to the north of the studied area, as the reference station (see Figure 3 and Tables S1 and S2 in the Supporting Information) to compare the January 2022 survey data with those of the previous surveys.

Aiming to build a detailed Bouguer anomaly map before the eruption, data observed in 2005 and 2021 were complemented with 274 gravity values from the Spanish IGN leveling network (140 around the Cumbre Vieja zone) (Figure 3). These gravity values are referred to as the absolute gravity values from IGN (Supporting Information, Table S2) and have an estimated precision of ~0.10 mGal. In addition, we used 1154 marine gravity values from the U.S. Geological Survey (USGS) to identify the offshore prolongation of land gravity anomalies. These data were collected by the Starella Research Vessel in 1987 and referred to the IGSN1971 standard gravity network, with line crossing differences of 1.1 mGal RMS [36,37].

Subsequently, the covariance analysis of the gravity map demonstrated the homogeneity among these gravity datasets and ensured a good transition between reference stations (Section 3.3).

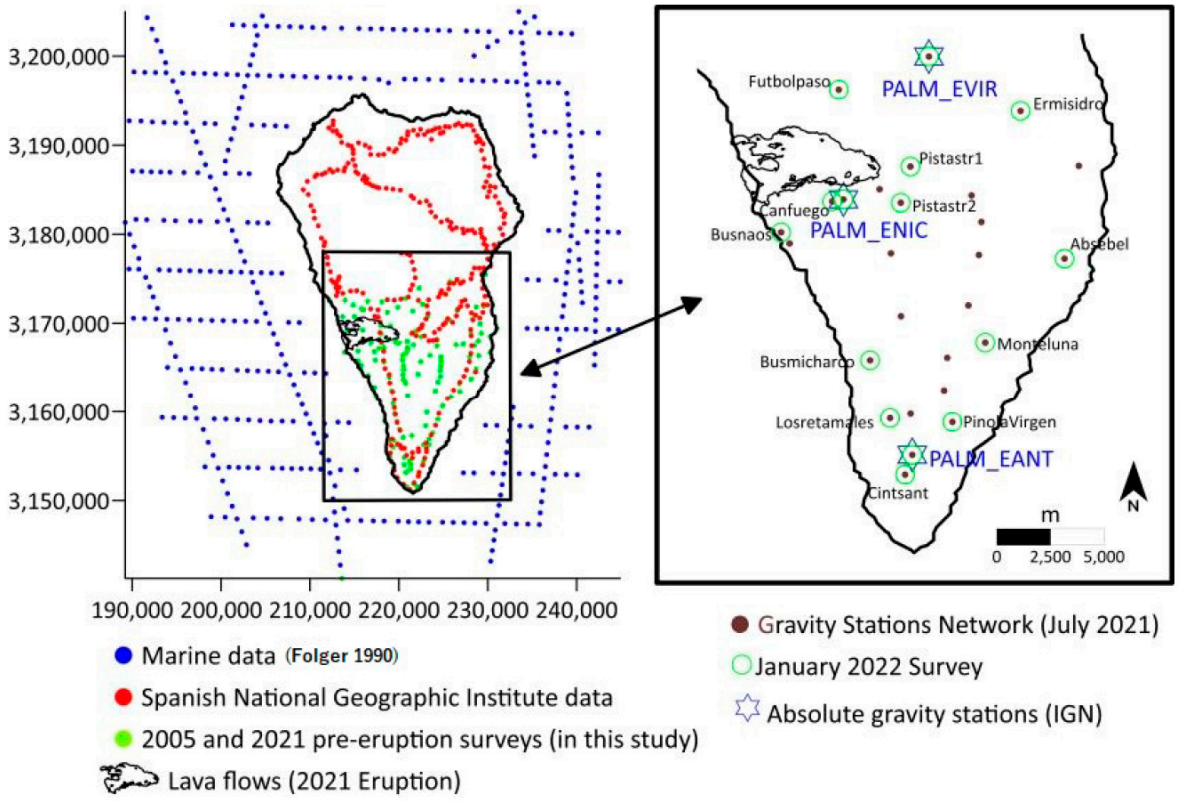

Figure 3. Distribution of the gravity stations of the different surveys used in this study. Marine gravity values are from the U.S. Geological Survey (USGS) [36]. The rectangular area shows an expanded image of Cumbre Vieja, where the names of absolute gravity stations (blue uppercase) and stations of the gravity network (black lowercase) are indicated. UTM coordinates are in m, in zone 28.

3.3. Bouguer Anomaly Map. Analysis of Gravity Anomalies and Inversion Algorithm

We used gravity data obtained before the 2021 eruption to calculate the Bouguer anomaly Δg_i^B for each *i*-station based on the equation

$$\Delta g_i^B = g_i^{obs} - g_i^N - \Delta g_i^{FA} - \Delta g_i^{Terr} - \Delta g_i^{Atm} \quad (1)$$

where the successive terms correspond to the observed gravity in the *i*-station, the normal gravity calculated for the GRS80 ellipsoid, the free-air reduction, the terrain correction and the atmospheric reduction due to the height of the station.

To calculate the terrain correction, the choice of an adequate density value that represents the average density of all topographic masses is critical. For this reason, we developed a comprehensive analysis based on the Nettleton method (Supporting Information, Section S3). Based on these results and focusing our study on the Cumbre Vieja area, we selected a mean density of 2450 kg/m^3 as the most representative density value for this area before the eruption of 2021 (Supporting Information, Figure S2). This value is similar to the density values calculated for other islands of the Canary archipelago (Supporting Information, Table S4), and it agrees well with the measured bulk density values (2412 $\pm$ 181 kg/m^3) obtained from basanitic and tephritic lava flow samples collected for this study, which can be considered representative of the shallower crust in this area (Supporting Information, Table S5).

The terrain correction calculated the effect of the topographic masses following a conventional method that defines different zones with different resolutions according to the distance from the station point. Both terrain and bathymetry data for the area around each observed point were modeled using prims distributed in a grid with six zones based on a grid, such as that proposed by [38], which extends up to a radius of 167 km. We used different digital elevation models (DEM) according to the zone of proximity. A DEM with 5 m of resolution is used to perform the near zone correction (1 to 50 m) and successive models with resolutions of 25, 50 and 500 m for the farther zones. Each zone of the grid defines a different prism size (Supporting Information, Table S3). All prisms have a density of 2450 kg/m^3 (1027 kg/m^3 is the water density value that is assumed in marine areas) with a bottom (top in marine areas) at level z = 0, and the height of each prism is defined as the orthometric height of its location for land areas and the bathymetric depth for oceanic areas. The prism gravity attraction value can be precisely calculated using Nagy's formula [39].

$$\Delta g_p^k = G\rho|||x_i \ln(y_i + r_i) + y_i \ln(x_i + r_i) - z_i \arcsin\frac{z_i^2 + y_i^2 + x_i y_i}{(y_i + r_i)\sqrt{z_i^2 + y_i^2}}|_{x_1}^{x_2}|_{y_1}^{y_2}|_{z_1}^{z_2} \quad (2)$$

The final Bouguer anomaly map displays anomalies in the range of 203 to 303 mGal (Figure 4) and shows a main gravity high over the Taburiente caldera. This feature could suggest a certain similarity with the topography. Obviously, the use of a constant density value for the terrain correction implies that a certain correlation could exist in areas of rugged topography, although this correlation is minimal according to the abovementioned Nettleton method. Nevertheless, all Canarian islands exhibit a similar pattern in their gravity maps (e.g., [16,40,41]), with a gravity high in the area where the seamount growth stage started. Moreover, the map exhibits a gradient zone with decreased gravity values toward the southern part of the island, where the main low is located. These gravity trends could mask significant features from local sources, which may be interesting to identify as signatures related to the 2021 eruptive process. According to Figure 4, the eruption occurred at the transition zone between the high and low gravity fields in the southern area.

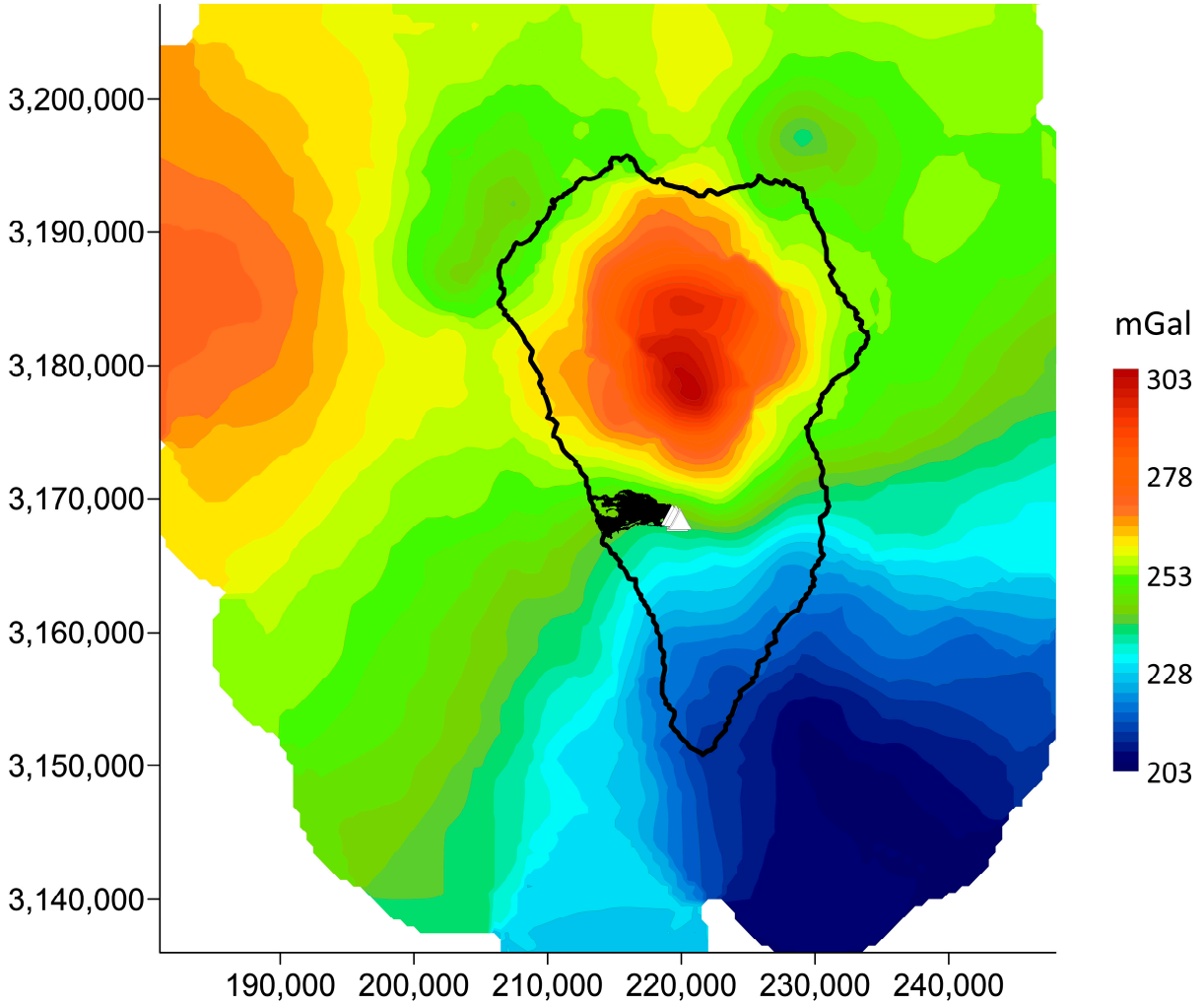

Figure 4. Bouguer anomaly map calculated from the gravity values observed before the 2021 eruption (Figure 3). The zone occupied by lava flows during the 2021 eruption is shaded in black, and the eruptive centers are indicated by white triangles. UTM coordinates are in m, in zone 28.

To quantify the consistency and homogeneity of different land and marine datasets used in obtaining the Bouguer map, we used a covariance analysis of the gravity data. If the information in these datasets is not uniform in composition or structure, a suitable covariance function cannot be found. Moreover, the covariance analysis and a further least-squares prediction permit us to obtain different levels of the gravity signal (e.g., [16]). We used this procedure to estimate the regional component of the gravity field obtained from the preeruption surveys (marine and land data; see Figure 3). Assuming that the covariance between two stations depends only on the horizontal distance, the empirical covariance is calculated and adjusted with a suitable analytical covariance function [42]. Then, the usual formulae for least-squares prediction [43] provide us with an estimation of a component of the gravity signal at this level of covariance. This estimated signal corresponds with the greatest amplitude component identified on the map, and therefore, it can be interpreted as a regional component associated with the deepest anomalous sources of the gravity field.

To study the influence of crustal structures on the occurrence of the 2021 eruption, the analysis was restricted to the area of Cumbre Vieja, where the epicenters of the earthquakes that occurred between July and December 2021 were located (Figure 5a). A clear coincidence between the occurrence of deep volcanotectonic earthquakes and the transition zone from high to low gravity values can be noted on the regional component map. After removing

this regional component from the observed gravity values, the result reveals local gravity field signatures associated with shallow masses (Figure 5b). Two main low-gravity zones are discernible on both sides of the Cumbre Vieja rift. Epicenters between 15 and 0 km in depth correlate with the western low-gravity zone, where the 2021 eruption took place. When applying the covariance analysis to this local anomaly, the estimated noncorrelated noise has a mean value of 0.001 mGal and a standard deviation of 0.365 mGal, which can be considered an estimation of the quality of the gravity map (Supporting Information, Figure S3).

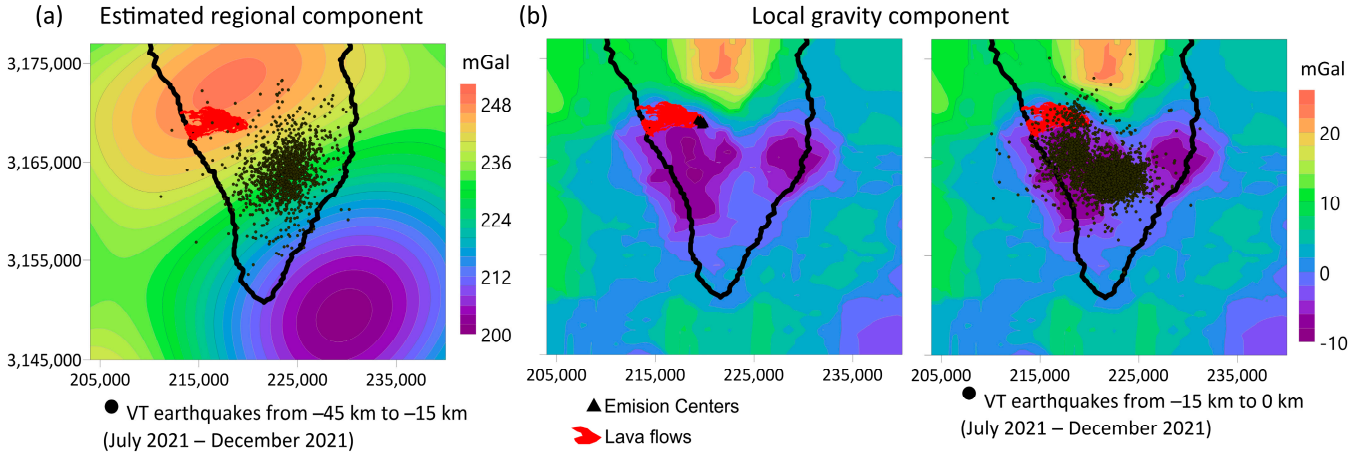

Figure 5. (**a**) Regional component of the gravity field estimated by covariance analysis. The horizontal distribution of deep volcanotectonic (VT) earthquakes is included. (**b**) Corresponding local gravity map calculated by removing the regional component from the observed gravity map without (center)/with (right) the horizontal distribution of shallow volcanotectonic events. UTM coordinates are in m, in zone 28.

The spectral analysis of the Bouguer anomaly map below the plane of observation based on Syberg's approach [44] revealed two different levels of sources at mean depths of 11.75 ± 0.70 and 2.16 ± 0.20 km (Supporting Information, Section S5 and Figure S4). Therefore, the identified regional component could represent the signature of structures located at the deepest level identified by the spectral analysis and could be related to the Moho, which is located at a depth of ~12 km [45].

The shallowest source level would be related to the local anomalies obtained after removing the regional component from the data (Figure 5). Consequently, the gravity inversion of these local anomalies can provide us with a model of the shallow structures that conditioned the path of the magma traveling to the surface during the 2021 eruption (Section 4.1).

Our gravity inversion approach, based on a genetic algorithm, has been successfully applied several times to search for the geometry of the gravity sources from a set of density contrast values fixed a priori. The methodology is fully explained in [16], and it involves simulating an evolutionary process of a population of possible solutions, $\mathbf{m}_k$, for the minimization of an error function given by

$$F(\mathbf{m}_k) = (\mathbf{A}\mathbf{m}_k - \mathbf{g}_{obs} - G_k\mathbf{u})^T \mathbf{E}_{ss}^{-1} (\mathbf{A}\mathbf{m}_k - \mathbf{g}_{obs} - G_k\mathbf{u}) + \beta \mathbf{m}_k^T \mathbf{C}_M \mathbf{m}_k \quad (3)$$

where $\mathbf{A}$ is defined by the forward problem, $\mathbf{E}_{ss}$ is defined by the data error, G_k is an average value of the gravity data, $\mathbf{u}$ is the unitary vector, β is a regularization parameter chosen a priori and $\mathbf{C}_M$ is the matrix that describes the uncertainty of model $\mathbf{m}_k$ [16].

Each model is defined by a 3D grid made of prisms with assigned density contrasts from selected a priori values, which are distributed from the surface to the deepest sections of the model, according to the radii of the survey area. Then, in an iterative process, the algorithm modifies a set of possible models that evolve by changing the density contrasts assigned to each cell, seeking to minimize the error function (3). After this evolutionary

process, where new generations of individuals are created and evaluated, the model that minimizes the error function is considered the best solution to the stated problem [16].

3.4. Gravity Changes between July 2021 and January 2022

During processes associated with eruptive events, the magma path and its storage system may cause both surface deformations and changes in the subsurface density distribution. These changes are likely to be detected as temporal gravity variations, which are observed in a network during different time periods of the volcanic process. In our case, the gravity network was configured according to site accessibility, which was limited due to the eruption process (Figure 2). Since our aim was to detect only subsurface mass changes, we accounted for two essential corrections to compare the gravity data acquired in the two surveys (July 2021 and January 2022): First, the gravimetric effect due to possible surface deformation during these periods (free-air effect), and second, the gravitational attraction of the new topography (the emitted lava flows and the new volcanic edifice). After these corrections, observed gravity changes should be associated only with the redistribution of subsurface masses. Additionally, a gravity gradient value is necessary for subtracting the vertical deformation effect from the data. Although it is known that the local gravity gradient may vary significantly across a volcanic area [46,47], it was not possible to measure it at each gravity station. Therefore, we used the global average value of −308.6 µGal/m to apply free-air correction (FAC) to the gravity values. The height changes between both surveys were determined from GNSS measurements made during the gravity surveys (Figure 6a). The results are consistent with the available data from the permanent GNSS stations (Figure 2) closest to the gravity benchmarks.

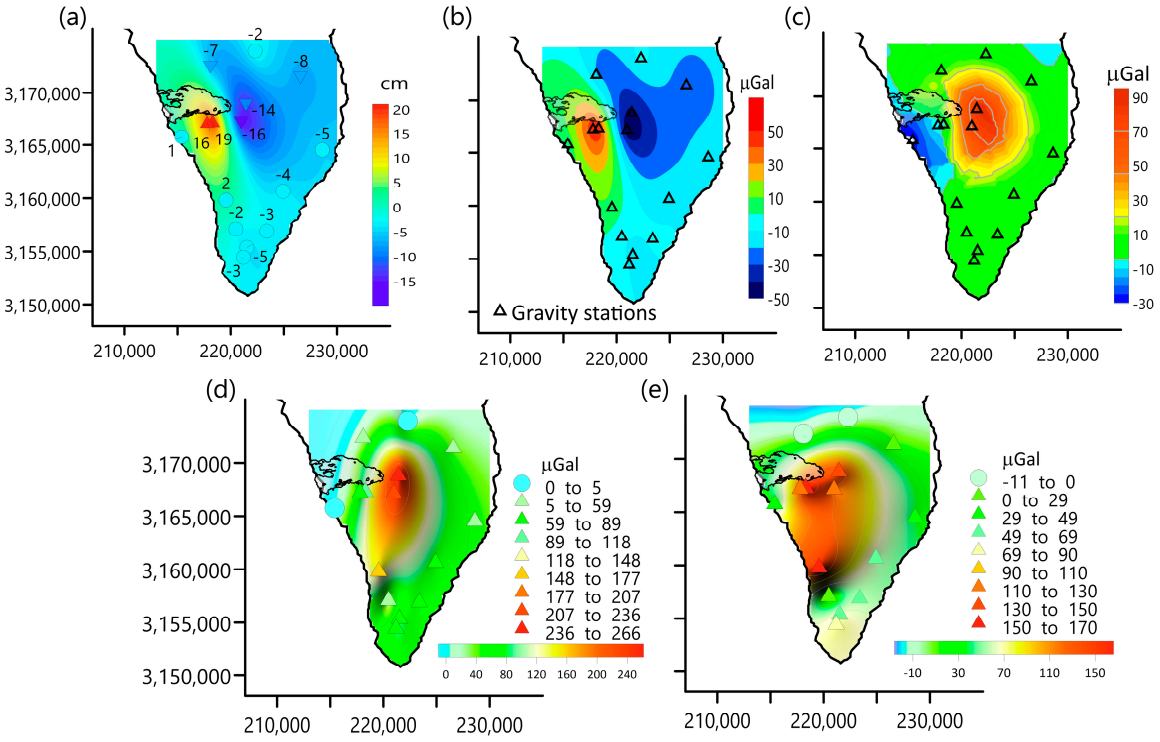

Figure 6. (**a**) Height differences observed between January 2022 and July 2021 as calculated through GNSS data processing observed in the gravity network. (**b**) Free-air correction for the gravity stations obtained from the height data (**a**). (**c**) Gravity attraction due to lava flows and the new volcanic edifices of the 2021 eruption. (**d**) Values of gravity differences calculated between January 2022 and July 2021. (**e**) Same results as (**d**) but considering the free-air correction and gravitational attraction of the new topography. Note that the contour maps shown in (**d**,**e**) are influenced by the distribution of a few gravity stations, showing predicted values where there are no data. UTM coordinates are in m, in zone 28.

The free-air correction (Figure 6b) shows the maximum correction (positive and negative) with amplitudes ranging from +54 to −45 μGal to the west and east, respectively, of the emission center. These positive and negative corrections run according to the deformation along the NNW–SSE direction and decrease with distance from the eruption zone.

The new topography generated by the eruption changed the local gravity field, affecting the values observed in January 2022. To quantify this effect, we used the elevation differences in the digital terrain model for the beginning and end of the eruption. This dataset is available through the Copernicus European program database (https://www.copernicus.eu/en (accessed on 1 July 2022). Section S6 in the Supporting Information includes the methodology used to calculate the new topography contribution to the gravity field. This gravity effect ranges from −28 to 112 μGal and depends on the assumed density of 3000 kg/m^3, which was based on grain density values obtained from the lava flows of the eruption (Supporting Information, Table S5) and on the proximity of the calculation point to the lava flows and the volcanic edifice originated by the 2021 eruption (Figure 6c and Figure S5 in the Supporting Information).

Figure 6d shows the gravity changes observed before and after the 2021 eruption in La Palma. Once the FAC and new topographic effects were removed, the gravity changes (Figure 6e) were presumably due to the redistribution of mass related to the eruptive process. The most remarkable feature on this map is a main high around the emission centers that runs SSW and has an elliptical shape.

3.5. Modeling of the Magmatic Plumbing System

Assuming that the migration of the hypocenters of the volcanotectonic events that occurred in the week preceding the eruption onset traced the path of magma ascent through the crust, we used the information reported in the IGN seismic catalog (https://doi.org/10.7419/162.03.2022 (accessed on 1 July 2022)) and a detailed spatiotemporal analysis of the relocated events provided by Del [48] to build an initial model of the plumbing system of the 2021 eruption. This model consists of a network of sills and dikes with geometric parameters obtained, on a first approximation, from the locations of the earthquake hypocenters. Once the horizontal and vertical sizes of the different elements that make up the model were determined, we estimated the thickness or maximum aperture for all of them. For this purpose, we used the method based on the aspect ratio of feeder dikes and sills proposed by [49,50]. A detailed description of the method can be found in the Supporting Information (Section S8). The details of this initial model are described in the Section 4.

The gravity changes observed in January 2022 with respect to July 2021 reflect the gravity attraction of the new masses emplaced within the volcanic edifice as the result of a shallow magma intrusion traveling to the surface. To better define the geometry and location of the elements of the initial model, we carried out forward modeling of the gravity increase detected after the eruption (Figure 6c).

To estimate the gravity attraction of this initial model, the sills and dikes were approximated by prisms of different sizes, dips and orientations and the analytical formulae for the gravity anomaly of a dipping prism of [51] were applied. We selected a mean density value of 3000 kg/m^3, which corresponds to the grain density values measured in samples of the 2021 eruption lava flows (Supporting Information, Table S5). As the dikes and sills are intrusive rocks with no porosity, the use of the grain density is more appropriate than the use of the bulk density, which is more representative of the scoriaceous part of the lava flows. The gravity attraction of each k-th element of the model, Δg_i^k, is calculated in the gravity network considering the station height. The sum of all effects provides us with the calculated gravity of the model at each i-station.

Starting from the initial configuration of sills and dikes (Section 4.2.2), we tested different values for the geometric parameters and location of the different elements to search for the best fit between the observed and calculated gravity values at the network points. Apart from small variations in these parameters and/or changes in their azimuths,

two new elements were added to obtain the best fit to the observed gravity data and to produce the final model of the magmatic plumbing system associated with the 2021 eruption at the Cumbre Vieja rift.

4. Results

4.1. Gravity Inversion Model for the Area of Cumbre Vieja Volcano

We applied the inversion procedure explained in Section 3.3 to the local gravity map (Figure 5b) to study the shallow structure beneath the Cumbre Vieja area. To define each model, the subsurface volume under the studied area was divided into a 3D grid made of 90,000 cubic prisms. The sides of the prisms gradually increase with depth, from 415 m for the shallowest prims to 900 m for the deepest prims at −15,000 m. Possible models of the sources of the gravity field were defined by allocating one of the a priori fixed-density contrasts, namely, −200, 0 and 300 kg/m^3, to each cell. The higher density contrasts correspond to dense mafic rocks (plutonic rocks or areas of high concentrations of basaltic dikes), whereas the lowest density contrasts correspond to highly weathered igneous rocks and/or clastic materials. Rocks with a null density contrast represent the typical subaerial volcanic products of Cumbre Vieja (lava flows and pyroclastic deposits). These density contrasts are based on the typical values for volcanic rocks of the Canary Islands (e.g., [52,53]) and are supported by other gravity studies in this area (e.g., [7,41]), as well as the density values obtained from rock samples in this work (Supporting Information, Table S5).

From an initial set of possible models (in this case, we selected a population of seven individuals), the algorithm acted iteratively by altering these models with mutation, cross and smoothness operators. Convergence was obtained after 216,000 iterations reached a fit to the gravity data, with a standard deviation of 0.8 mGal (Supporting Information, Figure S6), which was considered successful according to the estimated noise level of the data (Section 4.1).

Figure 7 shows the model of the distribution of density contrasts through several horizontal and vertical sections.

The shallowest horizontal slice (0 km depth) does not show any evident spatial trend, but several low- and high-density zones are distributed across the whole area. These likely correspond to the irregular distribution of different shallow volcanic products and structures (lava flows, cinder cones, ash-fall deposits, etc.). A more defined spatial distribution of the different density bodies appears with increasing depth (Figure 7). We identify a high-density zone located to the north and two low-density zones on both sides of the Cumbre Vieja rift, extending ~4 km downward. The high-density area, which has already been reported by [40], is consistent with the outcrop of the Pliocene seamount edifice and its associated plutonic complex at depth [12], which is also characterized by high resistivity [18]. The low-density body located to the west has the largest extent and displays a roughly NNW–SSE trend, as shown in the plane view. When the S–N and W–E vertical cross-sections are observed, a concave geometry appears in the upper part of this structure (Figure 7). The eastern low-density body is smaller in size and has an approximately circular shape, as shown in the plane view.

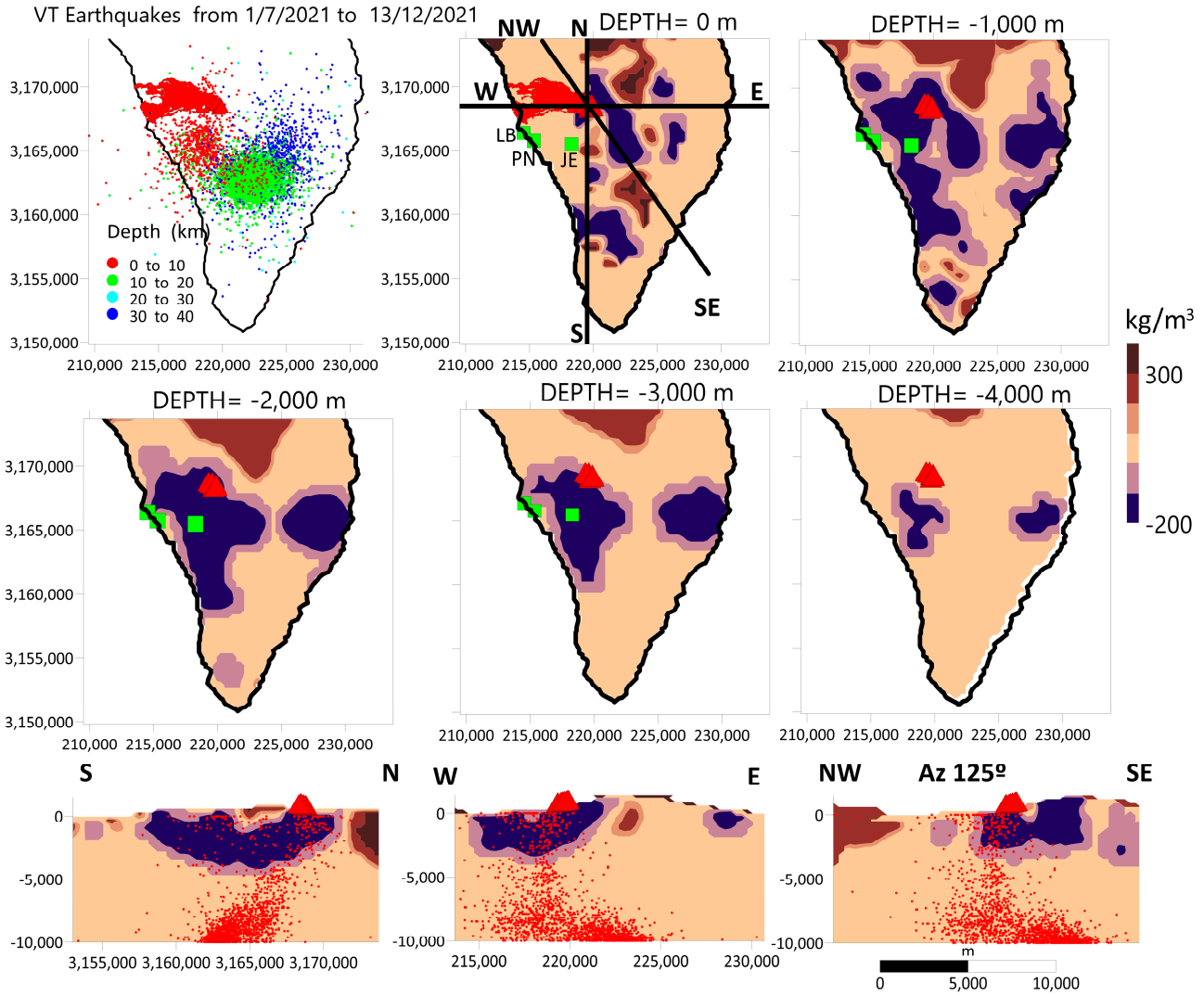

Figure 7. Model of the density contrasts obtained from the inversion of the local gravity map (Figure 5b) of the Cumbre Vieja area (La Palma). Density contrasts range between −200 and 300 kg/m^3. We show several horizontal sections at several depths and in three vertical sections (at the bottom of the figure) following the S–N, W–E and NW–SE directions, which are highlighted in the horizontal section at 0 km. The hypocenters of the volcanotectonic earthquakes that occurred from July to December 2021 are included. Red triangles indicate emission centers, the red polygon shows the area occupied by the lava flows during the 2021 eruption and green squares denote the villages of Puerto Naos (PN), La Bombilla (LB) and Jedey (JE). UTM coordinates are in m, in zone 28.

4.2. Geometry of the Crustal Magma Plumbing System for the 2021 Eruption

4.2.1. Initial Model from Seismic Data

The spatiotemporal distribution of the earthquakes that occurred in La Palma during the 2021 eruption (Section 3.5) allowed us to image the crustal magma plumbing system from a depth of 12 km to the surface (Figure 8). Seismicity was restricted to the upper 12 km of depth from 19 September to 1 October 2021 (Supporting Information, Figure S1). As determined from the energy spectrum analysis (Supporting Information, Section S5) and in agreement with previous seismic studies (e.g., [54]), this depth is consistent with the estimated location of the Moho discontinuity. Consequently, the seismicity developed during the preeruptive stage was entirely located between the Moho and the surface. Based on this information, we traced the path of magma through the crust, which we describe in

the following paragraphs and summarize in Table 1. All elements of this initial model are noted by a number and suffix I.

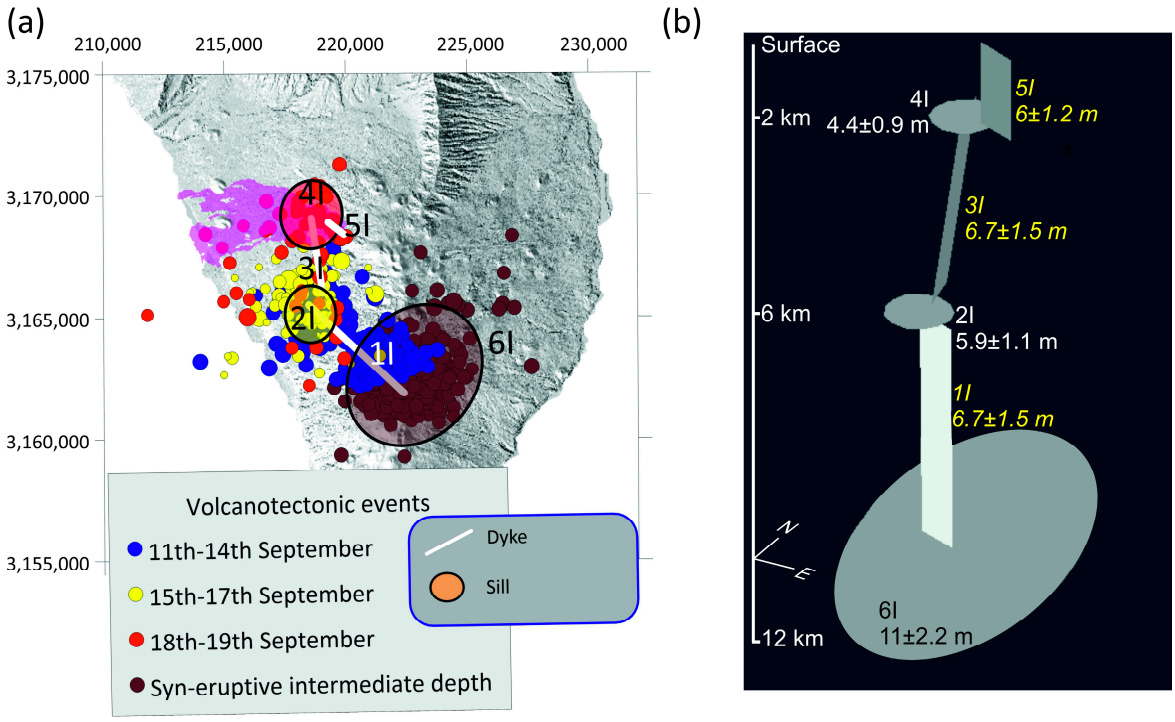

Figure 8. (**a**) Plane view of the spatiotemporal distribution of volcanotectonic earthquake events (m_{bLg} > 2) from 11–19 September 2021 and syneruptive intermediate-depth events. From this information, we produced an initial model of the magma plumbing system of the 2021 eruption consisting of different dikes (1I, 3I and 5I) and sills (2I, 4I and 6I). (**b**) Three-dimensional sketch of the model shown in (**a**). The values next to the labels correspond to the thickness of the sills and the width of the dikes. Details on the geometric properties of the elements of the model can be found in the text and in Table 1. UTM coordinates are in m, in zone 28.

Table 1. Geometric parameters of the sills and dikes of the initial model of the magma plumbing system obtained from the analysis of the recorded seismicity. The 'cross-sectional area/radius' shows the length and width of the dike cross-section and the radius of the surface occupied by each sill, assuming a circular/elliptical shape. The 'dip angle'/'azimuth' columns show the dip/orientation of the dikes (see Figure 8).

Element	Date	Center Coordinates		Cross-Sectional Area/Radius (m^2/m)	Depth (m)	Thickness (m)	Dip Angle	Azimuth (North)
		E-UTM	N-UTM					
1I-Dike	11–14 September	218,600	3,165,100	1000 × 6.7	(−12,000, −6000)		40°	133°
2I-Sill	15–17 September	218,600	3,165,100	1000	−6000	5.9		
3I-Dike	18–19 September	218,600	3,168,200	1000 × 6.7	(−6000, −2000)		55°	170°
4I-Sill	19 September	218,500	3,169,000	1700	−2000	4.4		
5I-Eruptive fissure	19 September	219,000	3,168,800	1000 × 6	(−2000, 1100)		90°	133°
6I-Sill	Eruptive period	222,700	3,162,950	2800	−12,000	11		

1—In the first four days after the beginning of the preeruptive seismic swarm (11–14 September), the volcanotectonic earthquakes define a dike propagating upward from depths of 12 to 7 km along a strike of N113°E and an ~40°SE dip angle (1I in Figure 8).

2—Over the next three days (15–17 September), seismicity stacked at a depth of 7 km, with a very small upward propagation (up to ~6 km) but extended radially up to ~2 km. This would be compatible with the development of an approximately circular sill of ~2 km in diameter with its top at a depth of ~6 km (2I in Figure 8). Immediately after this intermediate seismic swarm, some low-magnitude volcanotectonic events occurred approximately 3 km south at a shallower level (depth of ~1 km).

3—Suddenly, over a day and a half (18–19 September), seismic events started to propagate upward from depths of ~6 to ~2 km following a northward orientation, suggesting the intrusion of a new dike from the 6 km-depth sill that propagated in a N170°E direction with an ~55°S dip angle (3I in Figure 8).

4—After reaching a depth of ~2 km, seismicity expanded horizontally, first to the north and then east–west over an area of ~2 km in diameter that was very close to the place where, just a few hours later, the eruption started (19 September). We interpret the latter seismic activity as the emplacement of a sill-like shallow local magma reservoir (4I in Figure 8).

5—Small eruptive centers following a N133°E trend initially defined the eruptive fissure, and although different emission vents developed and disappeared over the 85 days of the eruption, the main orientation of the eruptive fissure remained almost constant. This would imply the intrusion of at least a final shallow dike connecting the local magma chamber to the surface, which can be defined by a subvertical dike (5I in Figure 8) trending N133°E with a length of at least 0.8–1 km along the strike, corresponding to the maximum distance between the different effusive centers that developed. At the end of the eruption, several vents opened on the southern part of the area covered by lava flows to the southwest of the volcano, and they opened 2 km away from the volcano in a NE–SW direction [55].

6—Soon after the eruption started, the seismicity at depths of ~12–14 km increased and remained almost constant during the whole eruptive process. The hypocenters define a tabular volume with a base area of ~ 7 × 2.5 km and a N40°E direction. We propose that this volume corresponds to the location of a sill-like body located at the Moho boundary (6I in Figure 8) resulting from the stagnation of magma ascending from the upper mantle that fed the upper system of interconnected sills and dikes (1I to 6I in Figure 8).

Taking all of this into account, the preliminary crustal magma plumbing system can be defined, from bottom to top, by a deep sill located at the Moho boundary feeding a deep dike trending N133°E that is connected to an ~2 km-diameter intermediate sill that is located at depths of ~6–7 km. A second dike trending N170° E would connect the sill with a shallower dike located only ~2 km depth below the eruptive fissure that is fed by a subvertical dike trending N133°E. This is a simplified model of an actual complex magma plumbing system consisting of several interconnected sills and dikes. Therefore, the potential presence of more dikes and sills at different places (such as that suggested by the shallow seismic swarm located to the SW of the study area) cannot be ruled out.

Regarding the estimates of the thickness or maximum aperture for each element of this model, the maximum opening displacement of the feeder dike originating at a depth of ~12 km and feeding the volcanic fissure associated with this eruption would be 6.7 ± 1.5 m. This value is of the same order of magnitude as that found in previous studies of feeder dikes in similar volcanic areas [50,56,57]. Regarding the different sills, we obtained maximum vertical thicknesses of 11 ± 2.2, 5.9 ± 1.1 and 4.4 ± 0.9 m for the 12, 6 and 2 km deep sills, respectively. Table 1 displays the geometric parameters defining the initial model of dikes and sills that describe the main features of the magma plumbing system based on a first approximation. A 3D view of the different elements of the model is shown in Figure 8.

4.2.2. Forward Modeling Using Gravity Data

The previous simplified model of dikes and sills was approximated by prisms of different sizes, dips and orientations, and they are listed in Table 2. The corresponding gravity attraction of this model (Figure 9) fits the observed gravity with a standard deviation of 42 μGal. Figure 9a reveals a gravity high of similar amplitude as that of the

observed gravity variation in the area around the eruptive center, although it is slightly shifted westward. However, the model does not reproduce the secondary gravity high of ~150 µGal detected in the SW zone of the study area. This gravity high shows a good spatial correlation with the diffuse shallow (~1 km) seismic swarm that occurred around 17 September (Section 4.2.1), suggesting that a secondary magmatic body that was not clearly imaged by the seismic data was located here. Consequently, this preliminary model does not reproduce the observed gravity variation exactly and must be refined (Figure 9c).

Table 2. Geometric parameters defining the elements of the initial model of the magma plumbing system used as starting points for gravity-forward modeling. These parameters are based on those displayed in Table 1 (deduced from the analysis of the seismicity), although they have been adapted to represent the sills and dikes as right and dipping prisms of the rectangular cross-section, respectively, for the calculation of their gravity attraction. Columns 'dx' and 'dy' show the lengths and widths of the top (and bottom) face of the prisms, respectively, whereas the azimuth column displays the orientation of these elements (see Figure 9).

Number	Element	Center Coordinates E-UTM	Center Coordinates N-UTM	dx (m)	dy (m)	Top (m)	Bottom (m)	Dip Angle	Azimuth
1I	Dike	218,600	3,165,100	1000	6.7	−6000	−12,000	40°	133°
2I	Sill	218,600	3,165,100	2000	2000	−5994	−6000	0°	0°
3I	Dike	218,600	3,168,200	1000	6.7	−2000	−6000	55°	170°
4I	Sill	218,500	3,169,000	2500	2500	−1996	−2000	0°	0°
5I	Eruptive fissure	219,000	3,168,800	1000	6	1100	−2000	90°	133°
6I	Sill	222,700	3,162,950	7000	4000	−11,989	−12,000	0°	40°

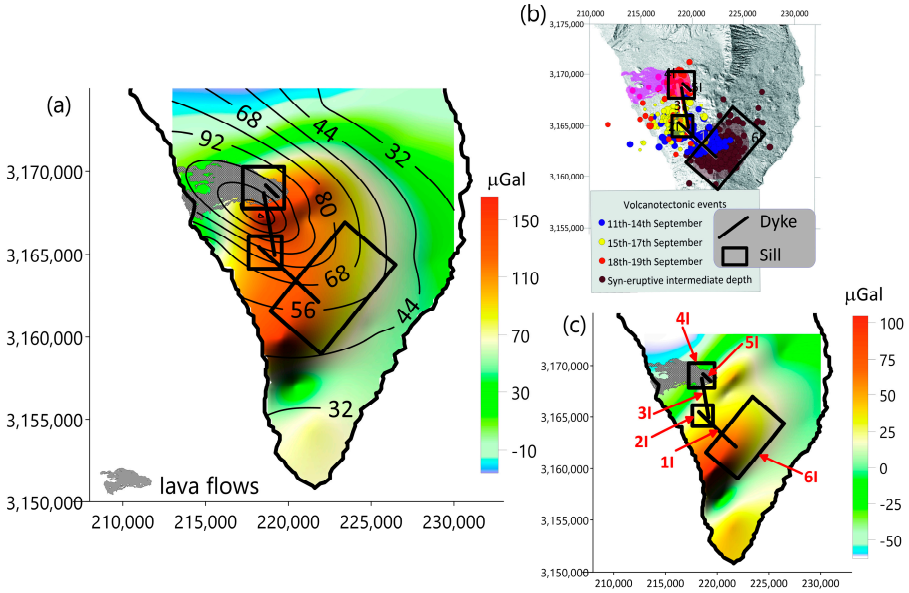

Figure 9. (**a**) Map of the gravity response due to the initial model of the magmatic feeding system (black contour lines) (Table 2), which should fit the gravity differences observed between January 2022 and July 2021 (filled colored contour map). (**b**) The sills and dikes were approximated by prisms (black lines and red labels in (**c**)) according to the locations of the volcanotectonic earthquakes. (**c**) Map showing the differences between the observed and calculated gravity values obtained by the interpolation of the data measured at the gravity stations. The maximum value (dark red spotted area) shows a gravity increase between surveys not justified by the gravity attraction of the sills and dikes of this initial model. UTM coordinates are in m, in zone 28.

To obtain a better fit of the gravity changes observed at the network stations, we tested small variations in the lateral dimensions and locations of the sills and dikes and/or changes in their azimuths. Moreover, we added two new elements to the preliminary model: a shallow (~1 km depth) sill of 2500 × 2500 m^2 in size and a feeder dike trending N–S connecting the shallow and intermediate (~6 km depth) sills (Table 3 and Figure 10). From the aspect ratio analysis explained in Section 3.5, the estimated sizes of these new elements (3F and 4F in Figure 10 and Table 3) are approximately 2.5 ± 0.5 m for dike 3F and 5 ± 0.9 m thick for sill 4F. The presence of these elements is also supported by the occurrence of seismic activity (Figure 8a) in the area.

Table 3. Parameters defining the final model of sills and dikes that best reproduce the temporal gravity increase associated with the emplacement of magma feeding of the 2021 eruption in La Palma. Note that the elements have been renumbered chronologically with respect to the initial model (Tables 1 and 2), adding the letter F had been added for 'final' instead of I for 'initial' and a new dike (3F) and sill (4F) have been added to the system. The geometric properties of the different elements of the model are displayed in Figure S9 of Supplementary Information S9.

Number	Element	Center Coordinates		dx (m)	dy (m)	Top (m)	Bottom (m)	Dip Angle	Azimuth (North)
		E-UTM	N-UTM						
1F	Dike	218,600	3,165,100	1000	7	−6000	−12,000	57°	133°
2F	Sill	218,600	3,165,100	2500	2000	−5994	−6000	0°	90°
3F	Dike	218,600	3,165,100	500	2.5	−1000	−6000	50°	170°
4F	Sill	218,500	3,160,200	2600	2600	−995	−1000	0°	0°
5F	Dike	218,600	3,168,200	1000	7	−2000	−6000	55°	170°
6F	sill	219,529	3,168,835	2500	2500	−1994	−2000	0°	145°
7F	Eruptive fissure	219,600	3,168,700	1000	6	1100	−2000	90°	133°
8F	Sill	223,300	3,162,500	7000	2500	−11,988	−12,000	0°	40°

Table 3 lists the final parameters of the model that best fit the observed temporal gravity increase detected by the gravity network. The final elements of the model are renumbered (followed by suffix F) in chronological order of emplacement to distinguish them from the initial model elements (followed by suffix I). Figures 10 and 11 show the elements of the new model, i.e., the calculated and the residual gravity fields, which were obtained by subtracting the calculated gravity from the observed data. The gravity residuals show the best fit for the observed data with a standard deviation of 29 μGal (Figures 10c and 11), which improves the gravity fit of the initial model gravity. It should be noted that we propose a model to justify the gravity increase observed after the volcanic process. This means that elements accounting for a gravity decrease or explaining very local (spatial or temporal) effects are not included in the model. For this reason, some gravity stations outside the modeled area display high negative residual values.

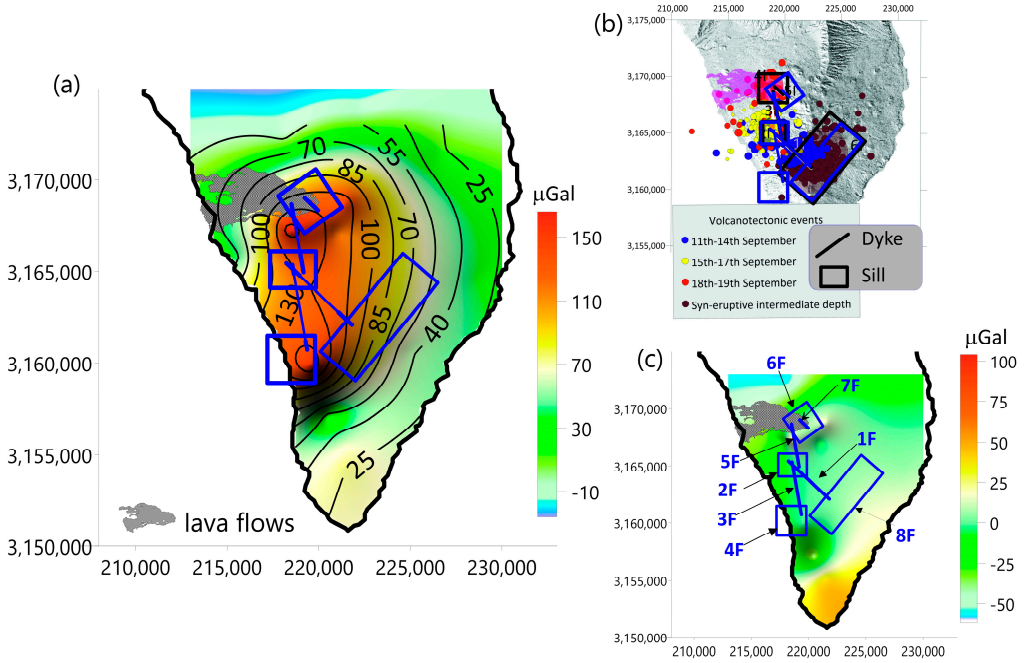

Figure 10. (**a**) Final model of dikes and sills (blue lines) inferred from forward gravity modeling. The gravity response of the model is shown as contour lines. Different dipping and right prisms (Table 3) were used to define the final model that best fits the increasing gravity values (filled contour map). (**b**) Comparison with Figure 9 to help identify the differences between the initial (black lines) and final (blue lines) models. (**c**) Map of the difference between the observed and calculated gravity values obtained from the values measured in the gravity network through interpolation.he color scale is the same as that used in Figure 9. UTM coordinates are in m, in zone 28.

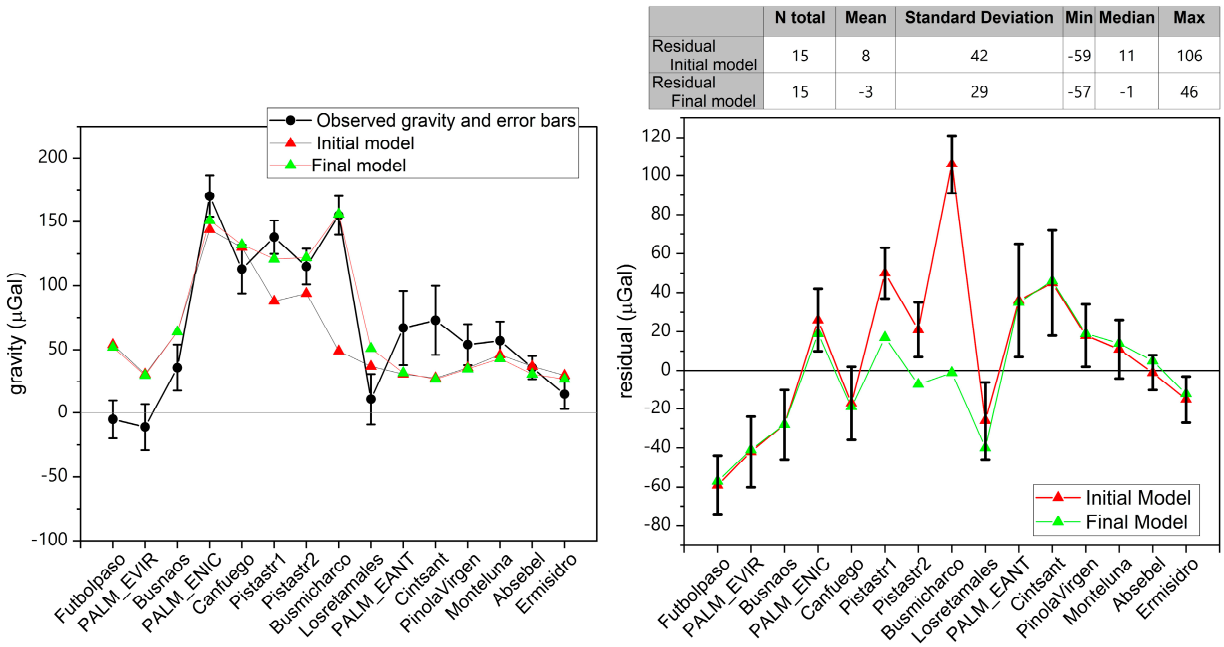

	N total	Mean	Standard Deviation	Min	Median	Max
Residual Initial model	15	8	42	-59	11	106
Residual Final model	15	-3	29	-57	-1	46

Figure 11. Comparison between gravity values (**left**) and residuals (observed gravity minus calculated gravity) (**right**) corresponding to the initial and final models. The observed gravity differences between January 2022 and July 2021 are displayed in black (**left**). Error bars indicate the errors estimated from the observed gravity values and free-air correction for each station. The statistical parameters are included in the table (**right**). The distribution of the gravity stations is indicated in Figure 3.

It is obvious that during the eruption at Cumbre Vieja, a complex process of movement and storage of magma would have taken place, making it very difficult to replicate all the possible elements involved in it in detail, especially given that we have only the previous and final gravimetric images of this process and no other syneruptive data. Moreover, other unconsidered local effects could be the cause of the gravity differences revealed by our network (for instance, differences in subsurface water storage linked to pluviometry or changes in hydrological conditions in local aquifers).

4.3. Surface Displacements from July 2021 to January 2022

The intrusion of igneous bodies at shallow levels within the crust produces deformations at the surface in the form of vertical and horizontal displacements that are measurable by means of geodetic techniques, mainly GNSS, InSAR and tiltmeters (e.g., [58]). As GNSS data were also acquired during the July 2021 and January 2022 gravity surveys, we used this dataset to test the accuracy and reliability of the proposed model of dikes and sills (Table 3) to reproduce the observed surface deformation (vertical uplift).

In this case, the joint inversion of the gravity and GNSS data would provide ambiguous results due to the inherent nonuniqueness of the gravity inversion solution limited by a scattered distribution of the data. For this reason, we propose to use a forward modeling approach by considering all seismic, gravity and displacement information to define the model and select the best solution according to its reliability.

We used Coulomb 3.4 software [59] to calculate the theoretical static vertical displacement caused by the dikes and sills of the magmatic plumbing system (Table 3). The software approaches the sources through tabular bodies to model a typical fault mechanism. Okada's dislocation model in an elastic half-space [60] gives the deformation and stress change caused by a tensile component of displacement, such as the opening or closing of a tabular body. We parametrized the dislocation model as having a given Young's modulus of E = 5 GPa, Poisson's ratio of σ = 0.25 and friction coefficient of 0.4. Assuming the dike expansion model described in Section 4.2.2., Figure 12 shows the Coulomb results for a depth of 0 km. Additionally, Figure 12b shows the comparison of these results with the vertical displacements at the gravity stations calculated from GNSS data observed during the July 2021 and January 2022 surveys (Figure 6a).

The resulting vertical displacement that was calculated by assuming the final model and using Coulomb 3.4 software is in good agreement with that obtained from GNSS data (Figure 12b). For instance, at the points closest to the eruptive zone where we made GNSS measurements, the vertical displacements were approximately +16 cm (Canfuego station) and +19 cm (PALM_ENIC station) to the west of the eruptive fissure, and the values changed to −14 (Pistastr1 station) and −15 cm (Pistastr2 station) to the east of the fissure (see Figure 3 for the distribution of stations). Similarly, the modeled vertical displacement varied from −20 to +20 cm around the eruptive zone. That is, gradual uplift of the surface appears to the west of the eruption, and in contrast, the eastern sector of the eruptive zone shows gradual subsidence in the same way that GNSS observations reveal. Therefore, this agreement between the different results for vertical displacement supports the proposed model of the magma plumbing system deduced from the distribution of volcanotectonic earthquakes and gravity data.

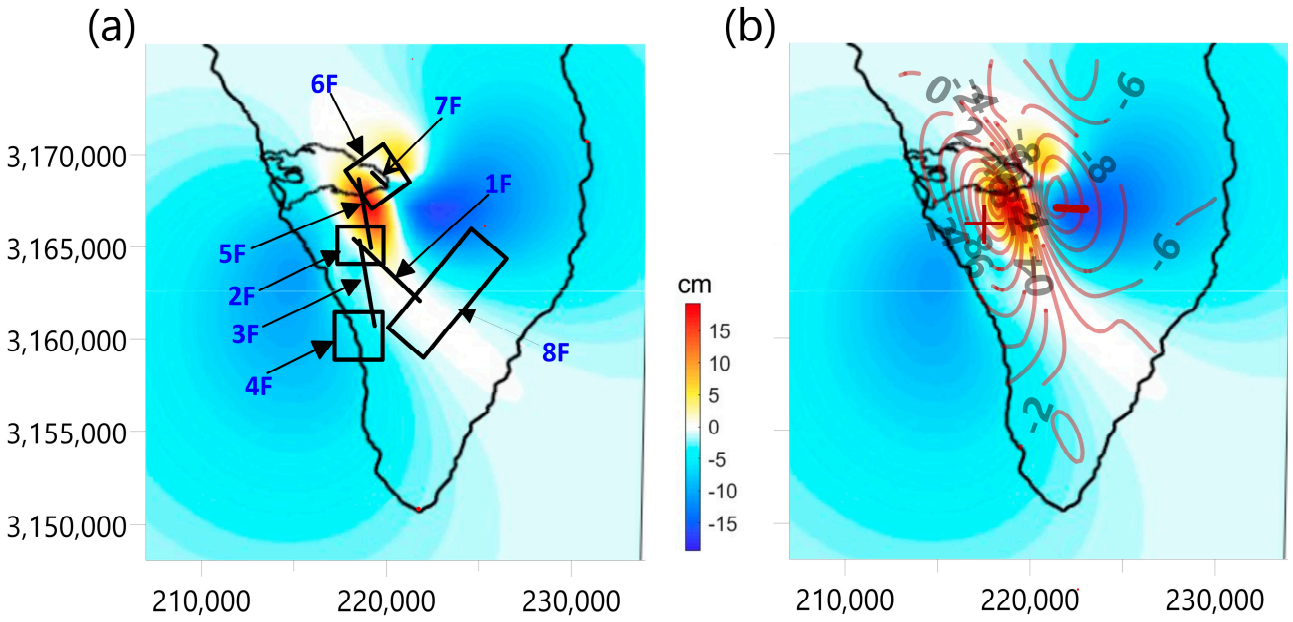

Figure 12. (**a**) Vertical displacement computed with Coulomb 3.4 software based on the modeled magmatic intrusions (Table 3). (**b**) Height variations (in cm) between January 2022 and July 2021 calculated from the processed GNSS observations obtained from the gravity network during the respective surveys, displayed as brown contour lines over the vertical displacement shown in (**a**). UTM coordinates are in m, in zone 28.

5. Discussion

A detailed image of magma plumbing systems and their temporal evolution is crucial to understanding how volcanic eruptions initiate and evolve over time, with important implications for the assessment of volcanic hazards [61]. The availability of different data observed during the volcanic process, such as the volcanotectonic earthquakes preceding and occurring during eruptive events (e.g., [62]) or the spatiotemporal gravity changes in the pre, syn and posteruptive phases (e.g., [63,64]), can significantly contribute to this knowledge.

In this work, the joint analysis of (1) the investigation of the preeruptive and syneruptive seismicity and (2) the forward modeling of the gravity changes produced during the eruption, as interpreted in the framework of the density distribution obtained through gravity inversion, represents a powerful tool for understanding the process of magma ascent and storage preceding the 2021 volcanic eruption in La Palma; this analysis provides us with a more detailed account of the process occurring below the surface compared to that obtained from the classical point source model estimations using idealized spherical or ellipsoidal cavities in an elastic half-space (e.g., Mogi model, [65–68], among others).

Density contrasts between the magma and crust can affect the material volumes extruded during a volcanic eruption [69] because they can act as a guide for magma ascent, both trapping magma [70] and favoring its ascent through boundaries where rheological changes are present [71,72]. Dense magmas can be trapped inside lower-density crustal areas depending on buoyancy levels and changes in rheological properties traversed during ascent. Low-density zones are usually explained by the existence of magma reservoirs under volcanic calderas [3,73], whereas high-density bodies under volcanic areas are usually related to zones where basaltic magma intrusions were intense in the past [7,74,75].

The inversion of the local gravity field (Figure 5b) revealed the inner structure of the upper part of the Cumbre Vieja volcanic edifice, where two main features can be distinguished (Figure 7): high-density structures that we interpret as intrusive bodies, such as mafic dikes and plutonic rocks, and low-density structures that we relate to highly

porous and permeable materials, such as pyroclastic deposits and/or highly weathered igneous rocks.

These low-density zones are in good agreement with the low-resistivity materials from 2 to 3.5 km below sea level inferred by [18], which were related to the presence of hydrothermal alteration products. In particular, the 2021 eruption occurred only at the northern boundary of the western low-density and low-resistivity body, which shows almost the same NW–SE trend as that of the eruptive fissure. This correlation suggests that the boundary of the low-density body (subvertical at the eruption location) corresponds to a major rheological contrast that would have conditioned the final magma path toward the surface (e.g., [76]). Moreover, the distribution of the shallowest volcanotectonic earthquakes, which points to this zone as a place where magma could accumulate (Figure 7) and the increase in the gravity values revealed by the survey carried out after the eruption (Figure 6) support this hypothesis.

Figure 13 shows an interpretative model of the structures identified by gravity modeling (Figure 7) and the evolution of magma upwelling from 11–19 September when it arrived at the surface (Figure 10). From the geological interpretation, some conclusions can be derived. The Moho interface constitutes a main rheological boundary where large sill-like bodies can be emplaced and act as temporary magma reservoirs, increasing pressure as the volume of accumulated magma increases. We propose that magma has accumulated (and differentiated) at least since the beginning of the seismic unrest detected in 2017 [29,77] and probably since 2009–2010 [15,78]. Figure 5a represents the component of the Bouguer gravity anomaly corresponding to the sources located in these deep sections. The high gravity anomaly gradient trending northwest/southeast encloses the seismicity at Moho depths, pointing to a high rheological contrast where high-density variation can trap magma.

Once magma overpressure reached a critical level (i.e., a value equal to or larger than the tensile strength of the crust at that depth), a dike began to propagate upward into the oceanic crust, as deduced from the migration of volcanotectonic earthquakes observed from 11–14 September. Dike propagation (element 1F in Table 3, Figures 10 and 13) continued until it reached the contact point between the old oceanic crust and the young submarine volcanic edifice (at ~6–7 km below sea level) because this lithological and rheological boundary constitutes a stress barrier [14,79]. There, the stagnation of magma developed a sill (element 2F) that accommodated the volume of melted material flowing from the Moho (second period in Figure 13). This intermediate-depth sill could not spread from 15–18 September except for a secondary dike that progressed southward. Indeed, the observed gravity changes reveal an increase in the gravity values in this zone, which can be explained only by mass addition beneath this area. We suggest that this anomaly was generated by the presence of a dike (element 3F) ascending through the low-density body toward the southwest part of the sill and becoming arrested at a depth of ~1 km below sea level, where a new sill developed (element 4F). It is worth noting that despite the dike reaching a very shallow depth, it failed to erupt, probably because the low-density body is made up of a soft, porous and permeable material (third period in Figure 13). Sills commonly form at the contact points between mechanically dissimilar rock layers (e.g., [50,80]), provoking the deflection of dikes into sills. Therefore, the occurrence of soft layers suppresses or reduces tensile stresses (e.g., [80]), causing the stagnation of the magma. This seems to be the case for these elements (dike 3F and sill 4F) that prevented an eruption in that zone that is located to the south of the village of Jedey (see Figure 1 for the location of Jedey). The lack of a neat seismic swarm associated with this sill can be explained by the fact that the soft material mainly deforms in a ductile manner and rarely develops the brittle deformation needed for the generation of volcanotectonic events.

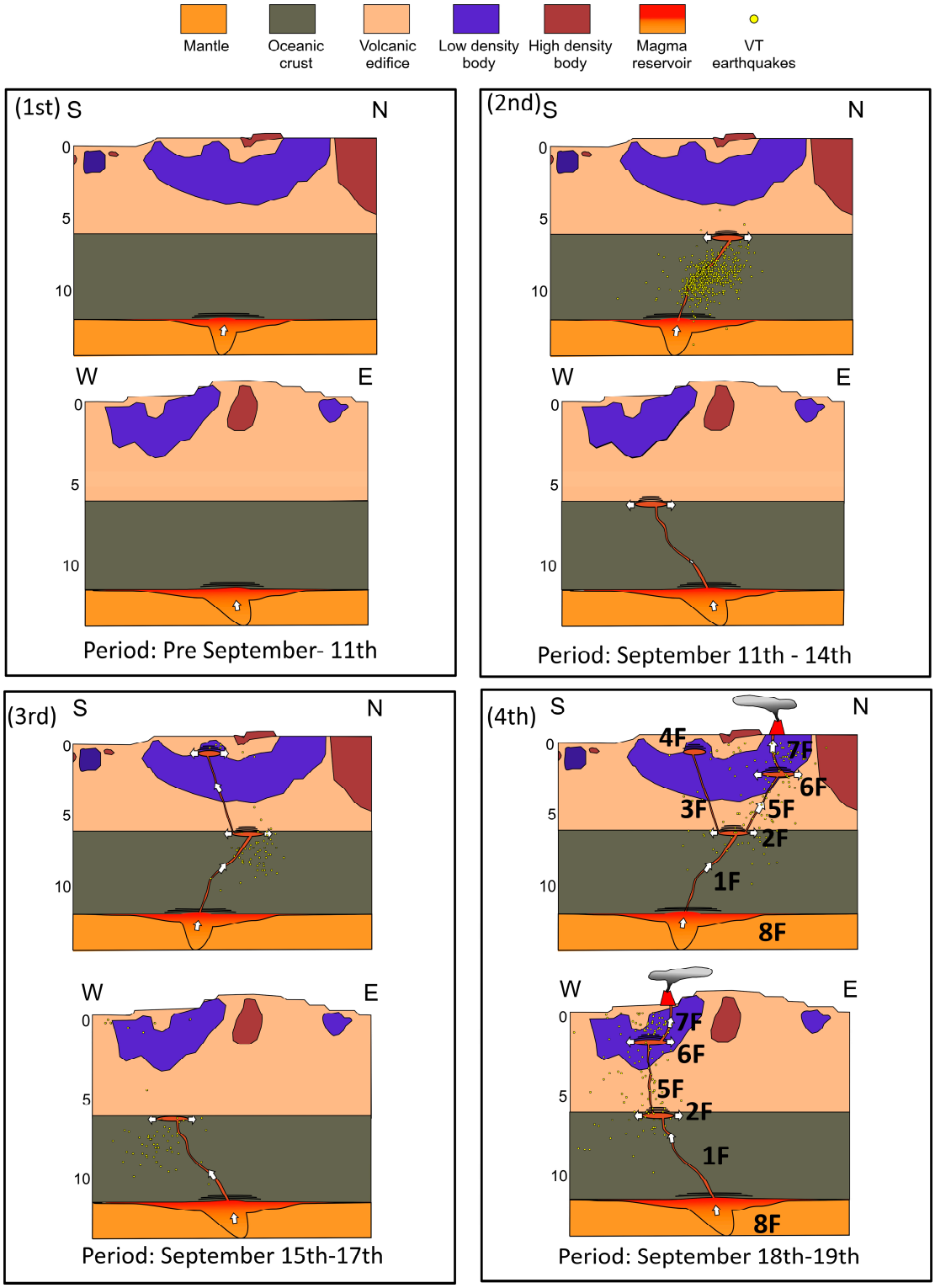

Figure 13. Distribution of the density contrast structures calculated from the gravity data inversion with the representation of the model of sills and dikes of the magma plumbing system (Table 3) during successive time periods before and until the onset eruption. The formation of sills (2F, 4F, 6F and 8F) at different horizontal boundaries and the path followed by dikes (1F, 3F, 5F and 7F) running through low-density structures support the hypothesis of the proposed model. The white arrows indicate the magma path. The distribution of volcanotectonic earthquakes shows a good correlation with the proposed model. The vertical scale is given in km.

According to [30], this is not the only previous attempt of magma ascent. Several ascending branches from a previous magma accumulation to the SSW of the final eruption vents occurred prior to the eruption between 13 September and 20 September 2021. Similar to the case corresponding to the south of Jedey, it corresponds to failed eruptions.

As long as the volume of the intermediate sill (element 2F) that was arrested at the base of the submarine edifice increased, on 18 September, magma overpressure forced a new dike (element 5F) to propagate upward from a depth of 6 km up to the boundary of the low-density body located at a depth of 2 km (fourth period in Figure 13), where a new shallow sill formed (element 6F). This sill is located only at the vertical northern boundary of the low-density body. In contrast to the shallow sill located south of the village of Jedey (element 4F) that could not propagate upward, the existence of this subvertical rheological discontinuity favored the upward progression of magma that finally reached the surface (element 7F) and caused the eruption on 19 September.

The different levels of magma stagnation obtained in this model agree with those obtained in thermobarometry studies for previous historical eruptions in La Palma (e.g., 1971 Teneguía, [81]; 1949 San Juan, [82,83]), favoring the hypothesis about the similarity among the magma plumbing systems of the historical eruptions in La Palma.

Our results suggest that the low-density structure plays a fundamental role, both in the process of magma ascent and in the final location of the eruptive vent. None of the shallow sills that formed because of the existence of the low-density body would finally succeed in producing an eruption. However, the sill beneath the eruption site was very close to the vertical boundary of the low-density body, favoring the fast propagation of accumulated magma and finally succeeding in reaching the surface, following the structural discontinuities that promoted this ascent [71,72].

The magnetotelluric study by [18] revealed the presence of a clay cap favoring the presence of an active hydrothermal system under Cumbre Vieja, where low resistivity values can be related to geothermal fluids. When the conductivity model of these authors is compared to our gravity inversion model, high spatial concordance between low-density volumes and low-resistivity anomalies can be noted.

The seismic tomography study carried out by [17] revealed low velocities for P and S seismic waves, which again highlights the soft features characterizing this area. The rheological change determined by the density, seismic velocities and resistivity contrasts affects magma buoyancy, whereas seismicity dispersion at this level would indicate an important rigidity contrast.

Notably, the surface area occupied by this low-density body associated with this volcanic process coincides well with the area where, before and during the eruption, successive episodes of inflation/deflation [31] were observed from GNSS and DInSAR data as well as significant variations in the corresponding baseline length (Figure 2). This reinforces our interpretation about how the presence of the low-density body conditioned the ascent of magma since trapping magma in its bottom section possibly caused inflation/deflation episodes due to the deflection of the ascending dikes into sills, whereas the low-density body favored magma ascent through its northern boundary. Considering that the low-density body represents a barrier for dike propagation, this would have implications for the assessment of the volcanic hazard in Cumbre Vieja, as the probability of a future eruptive event will be lower only in the area located over the low-density body. Conversely, the lateral subvertical boundaries of the low-density body constitute zones of preferential magma ascent, and thus, the probability of hosting future eruptive centers is higher there. This hypothesis would also apply to the location of previous historical eruptions. This seems to be the case for the San Juan 1949 eruption, with its eruptive center located just 2 km south of the 2021 Cumbre Vieja eruption and very close to the eastern boundary of the low-density body, but also for the Tajuya 1585 and El Charco 1712 eruptions.

Finally, the western boundary of the low-density body could also be the cause of the strong CO_2 concentrations affecting the villages of Puerto Naos and La Bombilla [32] that were previously described in Section 2. As shown in Figure 7, the western boundary of

the low-density body corresponds to a strong linear feature trending NW–SE connecting the location of the shallow (depth of ~1 km) sill (element 4F in Figures 10 and 13) to the evacuated villages. We propose that the degassing of the sill at depth is the origin of gas emissions that, favored by the high porosity and permeability of the low-density body and channeled through the contact between them and the dense rocks of the volcanic edifice, propagate NW, reaching the towns of Puerto Naos and La Bombilla. It is likely that CO_2 concentrations will remain high in these areas until the sill is fully degassed and solidified.

6. Conclusions

We analyzed the 2021 eruption at the Cumbre Vieja rift in La Palma using gravimetry techniques for both structural and spatiotemporal evolution purposes. Fresh data collected two months before the eruption's onset and immediately after its end provided us with new information about the subsurface structures involved in the process and the final mass redistribution produced by the eruption. Assuming that this volcanic process left a significant trace in terms of gravity changes, we used a combination of seismic and gravity information to obtain a detailed image of the shallow magma plumbing system that fed the 2021 eruption at Cumbre Vieja volcano.

The covariance and spectral analysis allowed us to separate the regional and local components of gravity, which are coherent with previous models developed from gravimetry and magnetotelluric sounding. The inversion of the local component of gravity to build a 3D density model of the shallow structures (Figure 7) revealed the presence of low-density structures, possibly linked to materials altered by the hydrothermal system.

We used spatiotemporal gravity data collected prior to and after the 2021 eruption to estimate the vertical displacement of the ground and changes in the gravity field associated with the mass increase for this eruptive event (Figure 6). These gravity and displacement data, which were analyzed jointly with preeruptive volcanotectonic seismicity, were used to build a forward model that contains simplified geometries representing a network of sills and dikes (Figure 10). This model describes a spatiotemporal framework that traces the path of magma ascent from the crust–mantle boundary to the surface from 11 September to 19 September 2021. Furthermore, the integration of this feeding system into our density model (Figure 7) revealed that a low-density body related to highly altered and porous materials controlled the magma path to the surface at shallow depths (see Figure 13).

In fact, our results suggest that the location of the eruptive vents of the 2021 eruption, and probably those of other historical eruptions in La Palma, were conditioned by the presence of the low-density body beneath the western flank of the Cumbre Vieja rift that prevented the ascent of magmas through it. When magma arrives at the base of this body, it becomes arrested and forms a sill. However, when the intrusion of magma takes place close to the boundaries of this body, it can succeed in propagating upward and reaching the surface because the rheological discontinuity associated with the contact between this body and the surrounding materials facilitates magma upwelling. This has important consequences for the assessment of volcanic hazards in La Palma since the probability of hosting future eruptive centers would be higher in the vicinity of the boundaries of the low-density body.

The magmatic system imaged by our data could also shed light on the current hazard produced by CO_2 concentrations affecting the villages of Puerto Naos and La Bombilla, as it is related to a shallow sill near the village area, which would be connected to the western boundary of the main low-density body identified in the proposed model.

Our results show that gravity studies, together with GNSS and seismic data, can provide us with significant insights into hazard warnings and risk assessments in volcanic areas. The shallow crustal model obtained from gravity inversion can help to identify the possible magma path and zones of stagnation during the volcanic process. Moreover, gravity control networks and other continuous monitoring techniques allow us to describe the temporal evolution of this process. Consequently, this work reinforces the importance

of using gravimetry and establishing denser control networks aimed at the continuous monitoring of the redistribution of masses produced during volcanic reactivation.

Supplementary Materials: The following supporting information can be downloaded at: https://www.mdpi.com/article/10.3390/rs15071936/s1, File: Supporting Information_Montesinos_FG.Pdf, Section S1: Spatiotemporal distribution of the earthquakes that occurred in La Palma during the 2021 eruption (Figure S1: Time series of the volcanotectonic (VT) earthquakes); Section S2: Gravity stations (Table S1: Geographic coordinates of the stations of the gravity network; Table S2: Absolute Gravity values from the gravity network of the IGN); Section S3: Terrain correction applied to the gravity data (Table S3: Features of the grid used for the terrain correction; Figure S2: (a) Map showing of the distribution of the density values; (b) Density values plotted vs the N coordinate; Table S4: Density values used in several studies to calculate the terrain correction in the Canary Islands); Section S4: Covariance analysis to identify the regional gravity component (Figure S3. Histogram of the final residuals of the covariance analysis); Section S5: Energy spectrum analysis of the gravity data (Figure S4: Logarithm of the power spectrum of the Bouguer anomaly); Section S6: Gravitational effect of the new topography on the gravity data (Table S5: Bulk and grain density values at Cumbre Vieja; Figure S5: Gravity effect induced by the new topography); Section S7: Gravity Inversion model (Figure S6: Histogram of the fit between the local gravity data and the calculated gravity from the inversion model); Section S8: Estimation of the width of the feeder dyke and related sills from aspect ratio analysis (Figure S7: Location of the VT events); Section S9: Model of the magma plumbing system for the 2021 eruption of Cumbre Vieja volcano (Figure S8: Geometric characteristics of the simple magma plumbing system model; Figure S9: Conceptual model of the inferred magma system). References [7,12,16,19,30,39–41,44,45,47,49,50,56,57,75,84–94] are cited in the Supplementary Materials.

Author Contributions: Conceptualization, F.G.M., J.A., S.S.-M. and D.G.-O.; methodology, F.G.M., S.S.-M., D.G.-O. and J.A.; software, F.G.M., S.S.-M. and D.G.-O.; validation, F.G.M., J.A., S.S.-M. and D.G.-O.; formal analysis, F.G.M., S.S.-M., D.G.-O., J.A. and I.B.-M.; investigation, F.G.M., J.A., S.S.-M., D.G.-O., I.B.-M., M.B., E.V., N.S. and T.M.-C.; data curation, F.G.M., S.S.-M., J.A., M.B. and E.V.; writing—original draft preparation, F.G.M., S.S.-M., D.G.-O. and J.A.; writing—review and editing, F.G.M., S.S.-M., D.G.-O., J.A., I.B.-M., M.B., E.V, N.S. and T.M.-C.; visualization, F.G.M., S.S.-M., D.G.-O. and J.A.; project administration, J.A.; funding acquisition, J.A. and F.G.M. All authors have read and agreed to the published version of the manuscript.

Funding: This research is supported by the project PID2019-104726GB-I00/AEI/10.13039/501100011033 funded by the Spanish Research Agency. Further, the University Complutense of Madrid (grants Financiación Grupos 2021, UCM 2022-GRFN14/22) and the Spanish Ministry of Science and Innovation (RD 1078/2021, funding for research activities of the CSIC-PIE project CSIC-LAPALMA-07) supported this research.

Data Availability Statement: The land gravity anomaly values used in this study were provided as supplementary data for the peer-review purpose. Upon acceptance, this dataset will be available from the Zenodo repository (https://doi.org/10.5281/zenodo.7539248 (accessed on 30 March 2023). The marine gravity data (https://doi.org/10.3133/mf2098B (accessed on 1 January 1990) were used under license for this study from U.S. Geological Survey [36]. The gravity data from IGN come from the levelling network established by this institution (the information can be consulted at https://visualizadores.ign.es/redes_geodesicas/ (accessed on 1 July 2022), they were used under license and can be requested from buzon-geodesia@mitma.es (IGN). The network gravity values observed between July 2021 and January 2022 (project PID2019-104726GB-I00/AEI/10.13039/501100011033) were provided as supplementary data for the peer-review purpose. Upon acceptance, this dataset will be available from the Zenodo repository (https://doi.org/10.5281/zenodo.7570284 (accessed on 30 March 2023).

Conflicts of Interest: The authors declare no conflict of interest. The funders had no role in the design of the study; in the collection, analyses, or interpretation of data; in the writing of the manuscript; or in the decision to publish the results.

References

1. Vajda, P. Recent developments and trends in Volcano Gravimetry. In *Updates in Volcanology—From Volcano Modelling to Volcano Geology*; Németh, K., Ed.; Intech: London, UK, 2016; pp. 81–103. eISBN 978-953-51-2623-2; ISBN 978-953-51-2622-5. [CrossRef]
2. Rymer, H.; Locke, C.A.; Brenes, J.; Williams-Jones, G. Magma plumbing processes for persistent activity at Poas volcano, Costa Rica. *Geophys. Res. Lett.* **2005**, *32*, L08307. [CrossRef]
3. Fedi, M.; D'Antonio, M.; Florio, G.; Paoletti, V.; Morra, V. Gravity modeling finds a large magma body in the deep crust below the Gulf of Naples, Italy. *Sci. Rep. (UK)* **2018**, *8*, 1–19. [CrossRef]
4. Kauahikaua, J.; Hildenbrand, T.; Webring, M. Deep magmatic structures of Hawaiian volcanoes, imaged by three-dimensional gravity models. *Geology* **2000**, *28*, 883–886. [CrossRef]
5. Rollin, P.J.; Cassidy, J.; Locke, C.A.; Rymer, H. Evolution of the magmatic plumbing system at Mt Etna: New evidence from gravity and magnetic data. *Terra Nova* **2002**, *12*, 193–198. [CrossRef]
6. Blanco-Montenegro, I.; Montesinos, F.G.; Nicolosi, I.; Arnoso, J.; Chiappini, M. Three-Dimensional MagneticModels of La Gomera (Canary Islands): Insights Into the Early Evolution of an Ocean Island Volcano. *Geochem. Geophys. Geosyst.* **2020**, *21*, e2019GC008787. [CrossRef]
7. Montesinos, F.; Arnoso, J.; Gomez-Ortiz, D.; Benavent, M.; Blanco-Montenegro, I.; Velez, E.; Crespo, T.; Gorbatikov, A.; Stepanova, M. Imaging the Volcanic Structures Beneath Gran Canaria Island Using New Gravity Data. *J. Geophys. Res. Solid Earth* **2022**, *127*, e2022JB024863. [CrossRef]
8. Mohamed, A.; Al Deep, M.; Abdelrahman, K.; Abdelrady, A. Geometry of the Magma Chamber and Curie Point Depth Beneath Hawaii Island: Inferences From Magnetic and Gravity Dat. *Front. Earth Sci.* **2022**, *10*, 847984. [CrossRef]
9. Maghfira, P.; Utami, P.; Niasari, S. Heat flow and gravity anomalies in some presumed hidden geothermal prospects in Java. *IOP Conf. Ser. Earth Environ. Sci.* **2022**, *1071*, 012025. [CrossRef]
10. Gailler, L.; Labazuy, P.; Dumont, Q.; Froger, J.L.; Peltier, A.; Finizola, A.; Cayol, V.; Chaput, M.; Régis, E.; The SlideVolc ERT Team. Volcano-magnetic signal reveals rapid evolution of the inner structure of Piton de la Fournaise. *J. Geophys. Res. Solid Earth* **2023**, *128*, e2022JB025290. [CrossRef]
11. Krastel, S.; Schmincke, H.U. Crustal structure of northern Gran Canaria, Canary Islands, deduced from active seismic tomography. *J. Volcanol. Geoth. Res.* **2002**, *115*, 153–177. [CrossRef]
12. Carracedo, J.C.; Rodriguez-Badiola, E.; Guillou, H.; Nuez Pestana, J.D.L.; Pérez Torrado, F.J. Geology and volcanology of La Palma and El Hierro, Western Canaries. *Estud. Geol.-Madr.* **2001**, *57*, 175–273.
13. Ancochea, E.; Hernán, F.; Cendrero, A.; Cantagrel, J.M.; Fúster, J.; Ibarrola, E.; Coello, J. Constructive and destructive episodes in the building of a young Oceanic Island, La Palma, Canary Islands, and genesis of the Caldera de Taburiente. *J. Volcanol. Geoth. Res.* **1994**, *60*, 243–262. [CrossRef]
14. Klügel, A.; Hansteen, T.H.; Galipp, K. Magma storage and underplating beneath Cumbre Vieja volcano, La Palma (Canary Islands). *Earth Planet Sci. Lett.* **2005**, *236*, 211–226. [CrossRef]
15. Fernández, J.; Escayo, J.; Hu, Z.; Camacho, A.G.; Samsonov, S.V.; Prieto, J.F.; Tiampo, K.F.; Palano, M.; Mallorquí, J.J.; Ancochea, E. Detection of volcanic unrest onset in La Palma, Canary Islands, evolution and implications. *Sci. Rep.* **2021**, *11*, 1–15. [CrossRef]
16. Montesinos, F.G.; Arnoso, J.; Vieira, R. Using a genetic algorithm for 3-D inversion of gravity data in Fuerteventura (Canary Islands). *Int. J. Earth Sci.* **2005**, *94*, 301–316. [CrossRef]
17. D'Auria, L.; Koulakov, I.; Prudencio, J.; Cabrera-Pérez, I.; Ibáñez, J.; Martinez, J.; Garcia-Hernandez, R.; Martínez van Dorth, D.; Hernandez, G.; Przeor, M.; et al. Rapid magma ascent beneath LaPalma revealed by seismic tomography. *Sci. Rep.* **2022**, *12*, 17654. [CrossRef] [PubMed]
18. Di Paolo, F.; Ledo, J.; Ślęzak, K.; van Dorth, D.M.; Cabrera-Pérez, I.; Pérez, N.M. La Palma island (Spain) geothermal system revealed by 3D magnetotelluric data inversion. *Sci. Rep. (UK)* **2020**, *10*, 18181. [CrossRef]
19. Lozano, G.; García, J.C.; Lorenzo, C.; Hernández, M.; Cabrera, A.; Díaz, E.; Camuñas, C.; Mediato, J.F.; López, J.; Pérez, R.; et al. (URGE-IGME Team). Mapa de Evolución de la Lava Entre el 24-11-2021 y el 14-12-2021. Available online: https://info.igme.es/eventos/la-palma/delimitacion-lava/211214_Evolucion-lava.pdf (accessed on 14 December 2021).
20. Albert, H.; Costa, F.; Martí, J. Years to weeks of seismic unrest and magmatic intrusions precede monogenetic eruptions. *Geology* **2016**, *44*, 211–214. [CrossRef]
21. Moss, J.L.; McGuire, W.J.; Page, D. Ground deformation monitoring of a potential landslide at La Palma, Canary Islands. *J. Volcanol. Geotherm. Res.* **1999**, *94*, 251–265. [CrossRef]
22. Perlock, P.A.; Gonzalez, P.J.; Tiampo, K.F.; Rodriguez-Velasco, G.; Fernandez, J. Time evolution of deformation using Time Series of differential interferograms: Application to La Palma Island (Canary Islands). *Pure Appl. Geophys.* **2008**, *165*, 1531–1554. [CrossRef]
23. Prieto, J.F.; Gonzalez, P.J.; Seco, A.; Rodriguez-Velasco, G.; Tunini, L.; Perlock, P.A.; Arjona, A.; Aparicio, A.; Camacho, A.G.; Rundle, J.B.; et al. Geodetic and structural research in La Palma, Canary Islands, Spain: 1992–2007 results. *Pure Appl. Geophys.* **2009**, *166*, 1461–1484. [CrossRef]
24. Arjona, A.; Monells, D.; Fernández, J.; Duque, S.; Mallorqui, J. Deformation analysis employing the Coherent Pixel Technique and ENVISAT and ERS images in Canary Islands. In Proceedings of the Workshop Fringe 2009, Frascati, Italy, 30 November–4 December 2009; European Space Agency: Paris, France, 2010; p. 8.

25. González, P.J.; Tiampo, K.F.; Camacho, A.G.; Fernández, J. Shallow flank deformation at Cumbre Vieja volcano (Canary Islands): Implications on the stability of steep-sided volcano flanks at oceanic islands. *Earth Planet Sci. Lett.* **2010**, *297*, 545–557. [CrossRef]
26. Escayo, J.; Fernández, J.; Prieto, J.F.; Camacho, A.G.; Palano, M.; Aparicio, A.; Rodríguez-Velasco, G.; Ancochea, E. Geodetic Study of the 2006–2010 Ground Deformation in La Palma (Canary Islands): Observational Results. *Remote Sens.* **2020**, *12*, 2566. [CrossRef]
27. Padrón, E.; Pérez, N.M.; Rodríguez, F.; Melián, G.; Hernández, P.A.; Sumino, H.; Padilla, G.; Barrancos, J.; Dionis, S.; Notsu, K.; et al. Dynamics of diffuse carbon dioxide emissions from Cumbre Vieja volcano, La Palma, Canary Islands. *Bull. Volcanol.* **2015**, *77*, 28. [CrossRef]
28. Padrón, E.; Pérez, N.M.; Hernández, P.A.; Sumino, H.; Melian, G.V.; Alonso, M.; Rodríguez, F.; Asensio-Ramos, M.; D'Auria, L. Early precursory changes in the 3He/4He ratio prior to the 2021 Tajogaite eruption at Cumbre Vieja volcano, La Palma, Canary Islands. *Geophys. Res. Lett.* **2022**, *49*, e2022GL099992. [CrossRef]
29. Torres-González, P.A.; Luengo-Oroz, N.; Lamolda, H.; D'Alessandro, W.; Albert, H.; Iribarren, I.; Moure-García, D.; Soler, V. Unrest signals after 46 years of quiescence at Cumbre Vieja, La Palma, Canary Islands. *J. Volcanol. Geoth. Res.* **2020**, *392*, 106757. [CrossRef]
30. Fernández, J.; Escayo, J.; Camacho, A.G.; Palano, M.; Prieto, J.F.; Hu, Z.; Samsonov, S.V.; Tiampo, K.F.; Ancochea, E. Shallow magmatic intrusion evolution below La Palma before and during the 2021 eruption. *Sci. Rep. (UK)* **2022**, *12*, 20257. [CrossRef] [PubMed]
31. De Luca, C.; Valerio, E.; Giudicepietro, F.; Macedonio, G.; Casu, F.; Lanari, R. Pre- and co-eruptive analysis of the September 2021 eruption at Cumbre Vieja volcano (La Palma, Canary Islands) through DInSAR measurements and analytical modeling. *Geophys. Res. Lett.* **2022**, *49*, e2021GL097293. [CrossRef]
32. Hernández, P.A.; Padrón, E.; Melián, G.V.; Pérez, N.M.; Padilla, G.; Asensio-Ramos, M.; Di Nardo, D.; Barrancos, J.; Pacheco, J.M.; Smit, M. Gas hazard assessment at Puerto Naos and La Bombilla inhabited areas, Cumbre Vieja volcano, La Palma, Canary Islands. In Proceedings of the EGU General Assembly Conference, Vienna, Austria, 23–27 May 2022; p. EGU22-7705. [CrossRef]
33. Arnoso, J.; Riccardi, U.; Tammaro, U.; Benavent, M.; Montesinos, F.G.; Vélez, E. 2D strain rate and ground deformation modelling from continuous and survey mode GNSS data in El Hierro, Canary Islands. In Proceedings of the 5th Joint International Symposium on Deformation Monitoring (JISDM), Valencia, Spain, 20–22 June 2022. [CrossRef]
34. Zumbergue, J.F.; Heflin, M.; Jefferson, D.C.; Watkins, M.; Webb, F. Precise Point Positioning for the Efficient And Robust Analysis of GPS Data from Large Networks. *J. Geophys. Res.* **1997**, *102*, 5005–5017. [CrossRef]
35. Arnoso, J.; Benavent, M.; Bos, M.S.; Montesinos, F.G.; Vieira, R. Verifying the body tide at the Canary Islands using tidal gravimetry observations. *J. Geodyn.* **2011**, *51*, 358–365. [CrossRef]
36. Folger, D.W.; McCullough, J.R.; Irwin, B.J.; Dodd, J.E.; Strahle, W.J.; Polloni, C.F.; Bouse, R.M. Map showing free-air gravity anomalies around the Canary Islands, Spain. In *Miscellaneous Field Studies Map*; MF-2098-B; United States Geological Survey: Resteon, VA, USA, 1990.
37. Morelli, C.; Gantar, C.; Honkasalo, T.; McConnell, R.K.; Tanner, I.G.; Szabo, B.; Uotila, U.; Whalen, C.T. *The International Gravity Standardisation Net 1971 (IGSN71)*; International Association of Geodesy: Paris, France, 1974.
38. Kane, M.F. A comprehensive system of terrain corrections using a digital computer. *Geophysics* **1962**, *XXVII*, 455–462. [CrossRef]
39. Nagy, D. The Gravitational Attraction of a Right Rectangular Prism. *Geophysics* **1966**, *31*, 362–371. [CrossRef]
40. Camacho, A.G.; Fernández, J.; González, P.J.; Rundle, J.B.; Prieto, J.F.; Arjona, A. Structural results for La Palma Island using 3-D gravity inversion. *J. Geophys. Res. Solid Earth* **2009**, *114*, B05411. [CrossRef]
41. Aparicio, S.S.; Martí, J.; Montesinos, F.G.; Gómez, A.B.; de Pablo, J.P.; Fernández, P.V.; García-Maroto, M.C. Gravimetric study of the shallow basaltic plumbing system of Tenerife, Canary Islands. *Phys. Earth Planet Inter.* **2019**, *297*, 106319. [CrossRef]
42. Barzaghi, R.; Sansò, F. Remarks on the inverse gravimetric problem. Geophys. *J. R. Astronom. Soc.* **1986**, *92*, 505–511.
43. Moritz, H. *Advanced Physical Geodesy*, 2nd ed.; University of Michigan: Dearborn, MI, USA; Wichmann: Karlsruhe, Germany, 1989; 500p.
44. Syberg, F.J.R. Potential field continuation between general surfaces. *Geophys. Prospect.* **1972**, *20*, 267–282. [CrossRef]
45. Ye, S.; Canales, J.P.; Rihm, R.; Dañobeitia, J.J.; Gallart, J. A crustal transect trough in the northern and northeastern part of the volcanic edifice of Gran Canaria, Canary Islands. *J. Geodyn.* **1999**, *28*, 3–26. [CrossRef]
46. De Zeeuw-van Dalfsen, E.; Rymer, H.; Sigmundsson, F.; Sturkell, E. Net gravity decreases at Askja volcano, Iceland: Constraints on processes responsible for continuous caldera deflation, 1988-2003. *J. Volcanol. Geotherm. Res.* **2005**, *139*, 227–239. [CrossRef]
47. Zahorec, P.; Vajda, P.; Papco, J.; Sainz-Maza, S.; Pablo, J. Prediction of vertical gradient of gravity and its significance for volcano monitoring—Example from Teide volcano. *Contrib. Geophys. Geod.* **2016**, *46*, 203–220. [CrossRef]
48. Del Fresno, C.; Cesca, S.; Klügel, A.; Domínguez Cerdeña, I.; Díaz-Suárez, E.A.; Dahm, T.; García-Cañada, L.; Meletlidis, S.; Milkereit, C.; Valenzuela-Malebrán, C.; et al. Magmatic plumbing and dynamic evolution of the 2021 La Palma eruption. *Nat. Commun.* **2023**, *14*, 358. [CrossRef] [PubMed]
49. Gudmundsson, A. *Rock Fractures in Geological Processes*; Cambridge University Press: Cambridge, UK, 2011; 578p.
50. Gudmundsson, A. *Volcanotectonics*; Cambridge University Press: Cambridge, UK, 2020; 586p.
51. Hjelt, S.E. The gravity anomaly of a dipping prism. *Geoexploration* **1974**, *12*, 29–39. [CrossRef]
52. González de Vallejo, L.; Hijazo Ramiro, T.; Ferrer Gijón, M. Engineering geological properties of the volcanic rocks and soils of the Canary Islands. *Soils Rocks* **2008**, *31*, 3–13. [CrossRef]

53. Rodríguez-Losada, J.A.; Hernández-Gutiérrez, L.E.; Olalla, C.; Perucho, A.; Serrano, A.; Eff-Darwich, A. Geomechanical parameters of intact rocks and rock masses from the Canary Islands: Implications on their flank stability. *J. Volcanol. Geotherm. Res.* **2009**, *182*, 67–75. [CrossRef]
54. Lodge, A.; Nippress, S.E.J.; Rietbrock, A.; García-Yeguas, A.; Ibáñez, J.M. Evidence for magmatic underplating and partial melt beneath the Canary Islands derived using teleseismic receiver functions. *Phys. Earth Planet. Inter.* **2012**, *212–213*, 44–54. [CrossRef]
55. Sanz-Mangas, D.; Galindo, I.; Pérez-López, R.; García-Davalillo, J.C.; Sánchez, N.; Rodríguez Pascua, M.A.; Perucha, M.A. Distal magmatic pulse injections at La Palma eruption 2021. In Proceedings of the Asamblea Hispano Portuguesa de Geodesia y Geofísica, Toledo, Spain, 28 November–1 December 2022.
56. Galindo, I.; Gudmundsson, A. Basaltic feeder-dikes in rift zones: Geometry, emplacement, and effusion rates. *Nat. Hazards Earth Syst. Sci.* **2012**, *12*, 3683–3700. [CrossRef]
57. Becerril, L.; Galindo, I.; Gudmundsson, A.; Morales, J.M. Depth of origin of magma in eruptions. *Sci. Rep.* **2013**, *3*, 2762. [CrossRef]
58. Dzurisin, D. *Volcano Deformation: New Geodetic Monitoring Techniques*; Springer Science & Business Media: Berlin, Germany, 2006. [CrossRef]
59. Toda, S.; Stein, R.S.; Sevilgen, V.; Lin, J. Coulomb 3.3 Graphic-rich deformation and stress-change software for earthquake, tectonic, and volcano research and teaching—User guide. *US Geol. Surv. Open-File Rep.* **2011**, *1060*, 63.
60. Okada, Y. Internal deformation due to shear and tensile faults in a half-space. *Bull. Seismol. Soc. Am.* **1992**, *82*, 1018–1040. [CrossRef]
61. Magee, C.; Stevenson, C.; Ebmeier, S.K.; Keir, D.; Hammond, J.; Gottsmann, J.H.; Whaler, K.A.; Schofield, N.; Jackson, C.; Petronis, M.S.; et al. Magma Plumbing Systems: A Geophysical Perspective. *J. Petrol.* **2018**, *59*, 217–1251. [CrossRef]
62. White, R.; McCausland, W. Volcano-tectonic earthquakes: A new tool for estimating intrusive volumes and forecasting eruptions. *J. Volcanol. Geotherm. Res.* **2016**, *309*, 139–155. [CrossRef]
63. Battaglia, M.; Roberts, C.; Segall, P. Magma intrusion beneath Long Valley caldera confirmed by temporal changes in gravity. *Science* **1999**, *285*, 2119–2122. [CrossRef] [PubMed]
64. Rymer, H.; Brown, G.C. Gravity fields and the interpretation of volcanic structures: Geological discrimination and temporal evolution. *J. Volcanol. Geotherm. Res.* **1986**, *27*, 229–254. [CrossRef]
65. Mogi, K. Relations between the eruptions of various volcanoes and the deformations of the ground surface around them. *Bull. Earthquake Res. Inst.* **1958**, *36*, 99–134.
66. Davis, P.M. Surface deformation due to inflation of an arbitrarily oriented triaxial ellipsoidal cavity in an elastic half-space, with reference to Kilauea volcano, Hawaii. *J. Geophys. Res. Solid Earth* **1986**, *91*, 7429–7438. [CrossRef]
67. Yang, X.; Davis, P.M.; Dieterich, J.H. Deformation from inflation of a dipping finite prolate spheroid in an elastic half-space as a model for volcanic stressing. *J. Geophys. Res. Solid Earth* **1988**, *7*, 934249. [CrossRef]
68. Fialko, Y.; Simons, M.; Khazan, Y. Finite source modeling of magmatic unrest in Socorro, New Mexico, and Long Valley, California. *Geophys. J. Int.* **2001**, *146*, 191–200. [CrossRef]
69. Hartley, M.; Maclennan, J. Magmatic Densities Control Erupted Volumes in Icelandic Volcanic Systems. *Front. Earth Sci.* **2018**, *6*, 29. [CrossRef]
70. Glazner, A.F.; Ussler, W. Trapping of magma at midcrustal density discontinuities. *Geophys. Res. Lett.* **1988**, *15*, 673–675. [CrossRef]
71. Sainz-Maza, S.; Arnoso, J.; Montesinos, F.; Marti, J. Volcanic signatures in time gravity variations during the volcanic unrest on El Hierro (Canary Islands). *J. Geophys. Res. Solid Earth* **2014**, *119*, 5033–5051. [CrossRef]
72. Marti, J.; Villaseñor, A.; Geyer, A.; Lopez, C.; Tryggvason, A. Stress barriers controlling lateral migration of magma revealed by seismic tomography. *Sci. Rep. (UK)* **2017**, *7*, 40757. [CrossRef]
73. Miyakawa, A.; Sumita, T.; Okubo, Y.; Okuwaki, R.; Otsubo, M.; Uesawa, S.; Yagi, Y. Volcanic magma reservoir imaged as a low-density body beneath Aso volcano that terminated the 2016 Kumamoto earthquake rupture. *Earth Planets Space* **2016**, *68*, 1–9. [CrossRef]
74. Gottsmann, J.; Camacho, A.G.; Marti, J.; Wooller, L.; Fernandez, J.; García, A.; Rymer, H. Shallow structure beneath the Central Volcanic Complex of Tenerife from new gravity data: Implications for its evolution and recent reactivation. *Phys. Earth Planet Int.* **2008**, *168*, 212–230. [CrossRef]
75. Sainz-Maza, S.; Montesinos, F.; Marti, J.; Arnoso, J.; Calvo, M.; Borreguero, A. Structural interpretation of El Hierro (Canary Islands) rifts system from gravity inversion modelling. *Tectonophysics* **2017**, *712*, 72–81. [CrossRef]
76. Maccaferri, F.; Bonafede, M.; Rivalta, E. A numerical model of dike propagation in layered elastic media. *Geophys. J. Int.* **2010**, *180*, 1107–1123. [CrossRef]
77. Longpré, M.A. Reactivation of Cumbre Vieja volcano. *Science* **2021**, *374*, 1197–1198. [CrossRef]
78. Day, J.M.D.; Troll, V.R.; Aulinas, A.; Deegan, F.M.; Geiger, H.; Carracedo, J.C.; Pinto, G.G.; Perez-Torrado, F.J. Mantle source characteristics and magmatic processes during the 2021 La Palma eruption. *Earth Planet Sci. Lett.* **2022**, *597*, 117793. [CrossRef]
79. Klügel, A.; Hansteen, T.H.; Schmincke, H. Rates of magma ascent and depths of magma reservoirs beneath La Palma (Canary Islands). *Terra Nova* **2003**, *9*, 117–121. [CrossRef]
80. Gudmundsson, A. Emplacement and arrest of sheets and dikes in central volcanoes. *J. Volcanol. Geotherm. Res.* **2002**, *116*, 279–298. [CrossRef]
81. Barker, A.K.; Troll, V.R.; Carracedo, J.C.; Nicholls, P.A. The magma plumbing system for the 1971 Teneguía eruption on La Palma, Canary Islands. *Contrib. Mineral. Petrol.* **2015**, *170*, 1–21. [CrossRef]

82. Klügel, A.; Schmincke, H.U.; White, J.D.L.; Hoernle, K.A. Chronology and volcanology of the 1949 multi-vent rift-zone eruption on La Palma (Canary Islands). *J. Volcanol. Geotherm. Res.* **1999**, *94*, 267–282. [CrossRef]
83. Klügel, A.; Hoernle, K.A.; Schmincke, H.U.; White, J.D.L. The chemically zoned 1949 eruption on La Palma (Canary Islands): Petrologic evolution and magma supply dynamics of a rift-zone eruption. *J. Geophys. Res. Solid Earth* **2000**, *105*, 5997–6016. [CrossRef]
84. Nettleton, L.L. Determination of density for reduction of gravimeter observations. *Geophysics* **1939**, *4*, 176–183. [CrossRef]
85. Camacho, A.G.; Montesinos, F.G.; Vieira, R.; Arnoso, J. Modelling of crustal anomalies of Lanzarote (Canary Islands) in light of gravity data. *Geophys. J. Int.* **2001**, *147*, 403–414. [CrossRef]
86. Camacho, A.; Montesinos, F.; Vieira, R. A 3-D gravity inversion by means of growing bodies. *Geophysics* **2000**, *65*, 95–101. [CrossRef]
87. Montesinos, F.G.; Arnoso, J.; Benavent, M.; Vieira, R. The crustal structure of El Hierro (Canary Islands) from 3-D gravity inversion. *J. Volcanol. Geotherm. Res.* **2006**, *150*, 283–299. [CrossRef]
88. Montesinos, F.; Arnoso, J.; Vieira, R.; Benavent, M. Subsurface geometry and structural evolution of La Gomera island based on gravity data. *J. Volcanol. Geotherm. Res.* **2011**, *199*, 105–117. [CrossRef]
89. Spector, A.; Grant, F.S. Statistical methods for interpreting aeromagnetic data. *Geophysics* **1970**, *35*, 293–302. [CrossRef]
90. Ranero, C.R.; Torne, M.; Banda, E. Gravity and multichannel seismic reflection constraints on the lithospheric structure of the Canary Swell. *Mar. Geophys. Res.* **1995**, *17*, 519–534. [CrossRef]
91. Murase, T.; McBirney, A. Properties of Some Common Igneous Rocks and Their Melts at High Temperatures. *GSA Bull.* **1973**, *84*, 3563–3592. [CrossRef]
92. Haimson, B.C.; Rummel, F. Hydrofracturing stress measurements in the Iceland research drilling project drill hole at Reydarfjordur, Iceland. *J. Geophys. Res. Solid Earth* **1982**, *87*, 6631–6649. [CrossRef]
93. Schultz, C.R.A. Limits on strength and deformation properties of jointed basaltic rock masses. *Rock Mech. Rock Eng.* **1995**, *28*, 1–15. [CrossRef]
94. IGN. Noticias e Informe Mensual de Vigilancia Volcánica. Available online: https://www.ign.es/web/resources/volcanologia/html/CA_noticias_2021.html#20211225 (accessed on 12 September 2021).